commercially known as "Ni-Hard 4", has very good abrasion resistance in aggressive chemical environments due to high levels of Ni content (between 3-7wt%). It has been shown that these alloys have superior atmospheric corrosion resistance to both the Cor-Ten Weathering steels and Hadfield manganese steels. Furthermore, resistance to pitting corrosion of abrasive wear resistant steels is improved by the addition of Ni.

Although in low alloy cast steels the beneficial effect of Mn on atmospheric corrosion has been reported, no significant effect was observed in cast irons.[25]

Due to the reasons discussed above, the addition of Mn, and Ni are examined in this study.

7.5.2 Results and Discussion

The experimental casts were made from high-purity elements, in an argon-arc furnace with a water cooled copper mould. It has been shown that the essential microstructures of these casts are comparable with those obtained by manual metal arc welding.[26] The chemical compositions of the alloys T1 (Fe-Cr-C-Mn), and T2 (Fe-Cr-C-Ni) are given in Table 7.5.

Table 7.5: Chemical compositions of the alloys T1 and T2 (wt%).

	Fe	Cr	C	Mn	Ni	Si
T1	balance	31.0	3.49	7.4	0.72	0.46
T2	balance	33.6	3.74	0.36	7.62	0.25

The optical micrographs of the alloys T1 and T2 (Fig. 7.20) showed that the microstructure consists of primary M_7C_3 carbides in the austenitic matrix with eutectic fine carbides as confirmed by TEM, and X-ray diffractometry. Microanalysis results indicate that the addition of Mn and Ni increases Cr concentration in the

austenitic matrix (Fig. 7.21-22, Table 7.6-7) compared with the Alloy 78. This is beneficial in terms of oxidation and corrosion resistance. However, quantitative measurements and thermodynamic calculations (which will be discussed later) showed that primary M_7C_3 volume fraction is lower than that of Alloy 78 particularly in Alloy T2. It is probable that this decrease gives rise to poor low-stress abrasion resistance. The results also show that Ni is completely dissolved into the matrix, and it hardly dissolves in the M_7C_3 carbides. Although, Ni increased the level of Cr in the matrix, compared with Alloy 78, this increase is not as much as with the Mn addition.
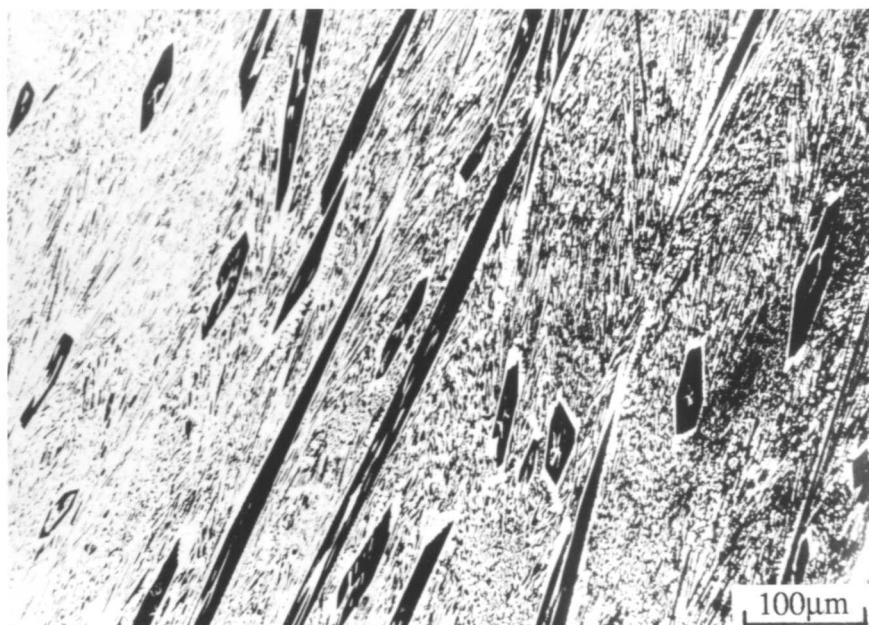
a

b

Fig. 7.20: Optical micrographs showing large primary M_7C_3 carbides in a eutectic mixture of γ +M_7C_3, a) Alloy T1; b) Alloy T2.
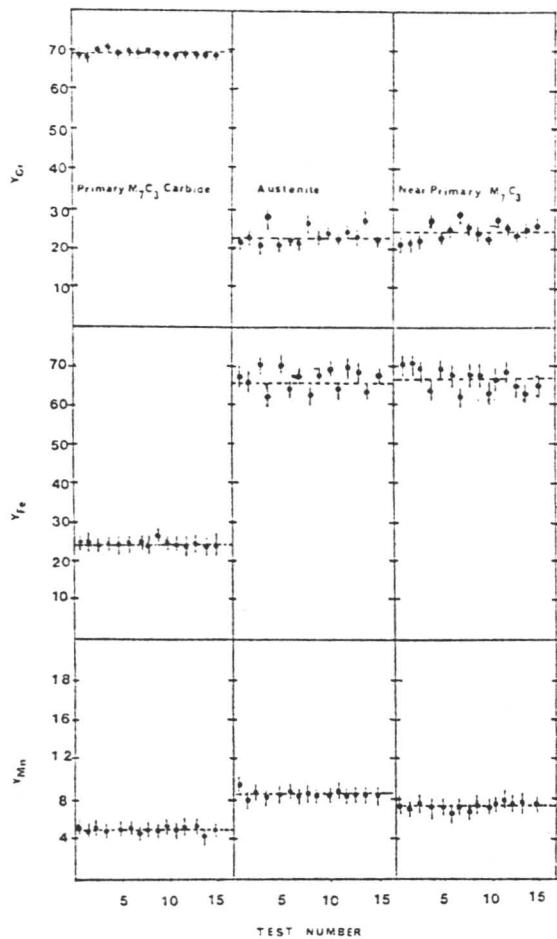
Fig. 7.21: Microanalytical data on primary M_7C_3, the austenite near the primary carbides and austenite in Alloy T1 when the carbon is not included (the continuous lines show the average values in each phase) at%.

Table 7.6: Mean composition of phases in alloy T1. The results are quoted to three decimal places for internal consistency. The results for the primary carbides and the austenite near the primary carbides (Near P. Carbide) are obtained using scanning electron microscopy.

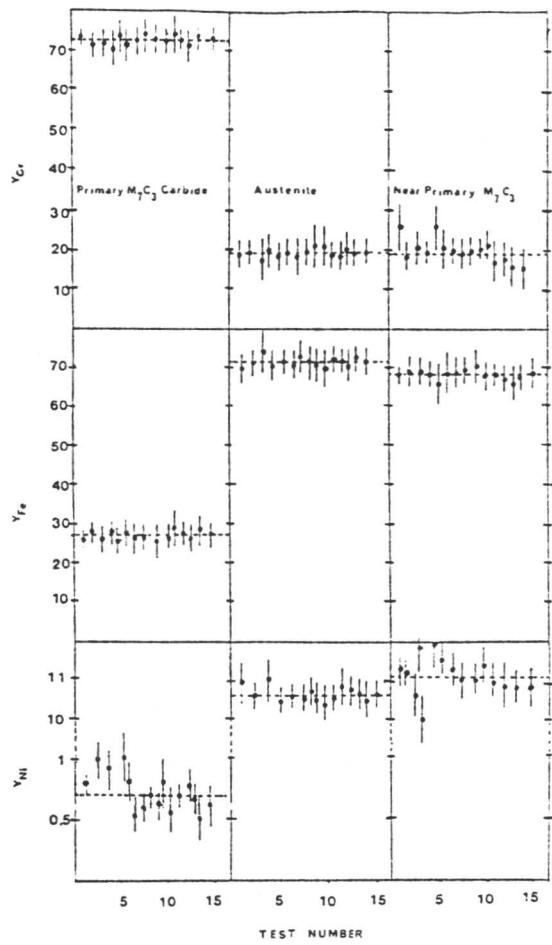|	Primary Carbide		Near P. Carbide		Austenite	
	Y_i	V_i	Y_i	V_i	Y_i	V
Fe	24.970	17.480	68.240	68.035	67.660	67.451
Cr	69.792	48.871	24.520	24.420	22.980	22.410
Mn	5.220	3.650	7.240	7.210	9.360	9.320
C		30		0.386		0.386

123

Fig. 7.22: Microanalytical data on primary M_7C_3, the austenite near the primary carbides and austenite in Alloy T2 when the carbon is not included (the continuous lines show the average values in each phase) at%.

Table 7.7: Mean composition of phases in alloy T2. The results are quoted to three decimal places for internal consistency. The results for the primary carbides and the austenite near the primary carbides (Near P. carbide) are obtained using scanning electron microscopy.

|	Primary Carbide		Near P. Carbide		Austenite	
	Y_i	V_i	Y_i	V_i	Y_i	V_i
Fe	26.955	18.870	68.427	64.550	70.155	66.180
Cr	72.420	50.710	19.683	18.562	19.232	18.140
Ni	0.625	0.437	11.890	11.210	10.613	10.010
C		30		5.690		5.690

Pin-on-disc abrasion, and single-pass scratch tests were carried out on both alloys. However, the results will be given for only the Mn containing alloy since detailed examinations of the worn surfaces of the two alloys revealed similar characteristics. Scanning electron micrographs of the pin-on-disc wear scars of the alloy T1 caused by SiC and Al_2O_3 abrasives are given in Fig. 7.23. The micrographs after single-pass scratch tests at 500g and 1kg using a Vickers pyramidal diamond are shown in Fig. 7.24. The pin-on-disc abrasive wear test results showed that the scratch groove dimension is the same as in the Alloy 78, implying no contribution of Mn and Ni to abrasive wear resistance. SEM micrographs of the worn surfaces show that the carbides are worn at the same level as the matrix, leaving pits at the carbide/matrix interfaces. Scratch test results at 500g and 1kg using a Vickers pyramidal diamond showed that the matrix with eutectic carbides are ploughed into both edges of the scratch groove. Furthermore, carbide cracking at the carbide/matrix interfaces are extensively observed.

The results indicate that despite the beneficial effects of Mn, and Ni in increasing Cr concentration of the matrix, these elements have almost no influence on abrasive wear resistance of high Cr containing Fe-based hardfacing alloys particularly in heavy abrasive wear conditions.

7.5.3 Conclusions

An attempt has been made to stabilise the austenite in the matrix of high Cr containing iron-based hardfacing alloys. The microstructures of the experimental casts were found to contain primary M_7C_3 carbides and the eutectic mixture of austenite and M_7C_3 carbides. Microanalysis experiments showed that Mn and Ni increases the Cr concentration of the austenitic matrix compared with the Alloy 78. However, the volume fraction of primary carbides is lower than that of Alloy 78. This decrease is probably associated with either a thermodynamic effect of Mn and Ni, or lower carbon concentration of the Mn and Ni containing alloys.

Pin-on-disc abrasion and scratch test experiments showed that carbides are spalled off leaving behind a pitted surface. Scratch groove dimensions in the eutectic mixture and primary carbides are the same indicating that primary carbides do not contribute significantly to wear resistance. The results confirm that the effect of Mn and Ni are negligible, as far as the heavy abrasive wear resistance is concerned.
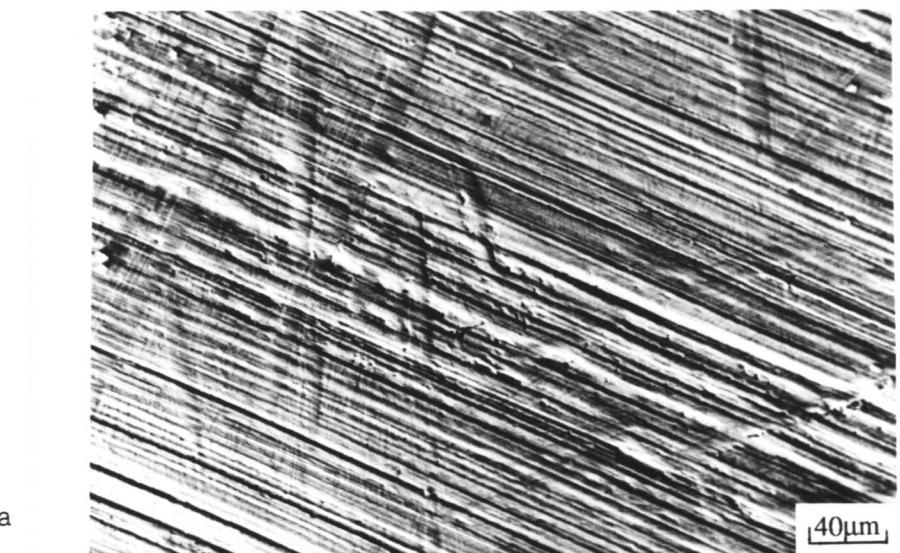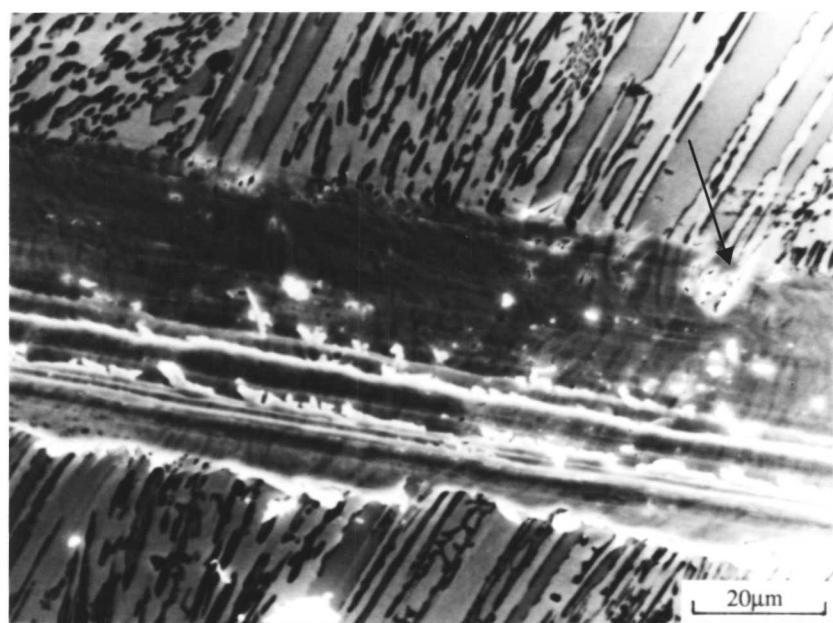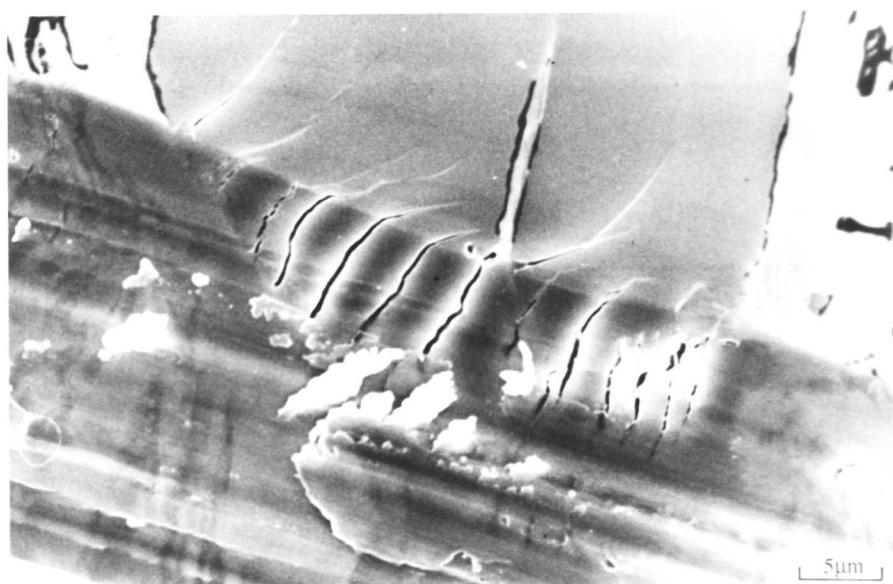
a

40µm
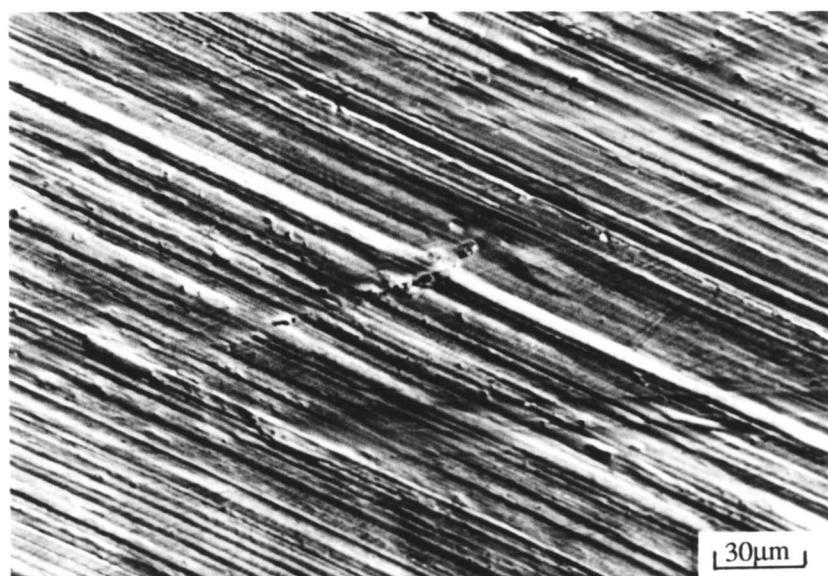
b

30µm

Fig. 7.23: Scanning electron micrographs of the worn surfaces of alloy T1 after the pin-on-disc abrasion test using a) SiC (220 mesh) abrasives at 1kg load; b) Al_2O_3 (400 mesh) at 450g, showing that carbides are worn to the same level as the eutectic mixture.

a

b

Fig. 7.24: Scanning electron micrographs of the alloy T1 after single-pass-scratch tests; a) at 500g showing carbide cracking (marked by arrow), also note that there is no difference in the scratch groove dimension between the primary carbides and the eutectic phase; b) at 1kg showing carbide cracking which probably initiated at the carbide-matrix interface.

127

7.6 Effect of Si on the Microstructure and Abrasive Wear Resistance

7.6.1 Introduction

The diffusional transformation of γ to α +M_7C_3 in Alloy 78 may not significantly influence the wear resistance, but it might alter the corrosion and oxidation resistance of the alloy since the resulting α has a reduced chromium concentration. Of course, as far as the M_7C_3 is concerned, its Cr concentration ($\approx$45at.%) is more than adequate for corrosion and oxidation resistance. A major aim of the present work was to design a Fe-Cr-C-based alloy which has a better matrix corrosion and oxidation resistance at all service temperatures even following the inevitable diffusional transformations. It was proposed to achieve this by adding high levels of silicon, which is known to have a very low solubility in carbides[27] (and specifically, also in M_7C_3[28]). Hence, most of the silicon in the alloy, should during solidification be partitioned into the liquid phase, and subsequently (during the eutectic transformation) into the austenite, giving a much enhanced level of Si. There are several advantages in this; Si is known to enhance the oxidation and corrosion resistance of iron[29] and it increases the volume fraction of M_7C_3 carbides in high Cr containing steels.[30] Furthermore, if the austenite subsequently transforms to ferrite and M_7C_3, then the Si concentration of the ferrite should be even higher, so that oxidation resistance should be enhanced. It was also anticipated that Si may refine the carbides in the microstructure; such an effect is well established for high strength steels.[27] At the same time, any influence of further alloy additions on the partitioning of Cr between the M_7C_3 and matrix also needed to be investigated; any change may influence the volume fraction of hard phase and therefore wear properties.

In an effort to improve the high-temperature stability, oxidation and corrosion resistance of such hardfacing alloys, a systematic study has been carried out on the role of Si on the microstructure, phase chemistry and abrasive wear resistance of Fe-Cr-C-based alloys. The investigations have been carried out on model alloys cast by an argon arc melting technique, which is in general found to simulate adequately the corresponding structures obtained by manual metal arc welding. The chemical compositions of the alloys are given in Table 7.8.

Table 7.8: Chemical compositions of Fe-C-Cr-Si alloys, in weight %.

| No.	C	Cr	Mn	Si
S1	3.90	33.6	0.00	0.20
S2	4.48	34.4	0.00	3.60
S3	3.60	31.2	0.00	6.90

7.6.2 Results and Discussion

Much of the initial work has been carried out on the experimental 65g melts discussed earlier, because the design of suitable welding electrodes is a more complex problem. It was therefore felt necessary to check that the essential microstructures of experimental welds compared well with those obtained by manual metal arc welding.

Alloy S1 is essentially of the same composition as Alloy 78; the slightly lower carbon and chromium concentrations of S1 should not significantly influence the nature of the γ or M_7C_3, although the volume fraction of M_7C_3 should be lower in S1. Optical microscopy (Fig. 7.25) demonstrated that the alloys have identical microstructures; microanalysis results (Fig. 7.26, Table 7.9) show that the austenite in S1 has a higher Cr content, and this is consistent with the fact that the casting technique involves a somewhat higher cooling rate than that associated with arc welding. This would mean that the alloy becomes configurationally frozen at a higher temperature, where the Cr concentration in γ in equilibrium with M_7C_3 is expected to be higher. With this exception, the results show that argon arc melts can be used in simulating manual metal arc weld deposits, especially for revealing trends in microstructure and phase composition.

Optical micrographs of alloys S1, S2 and S3 show that a major effect of silicon is to change the morphology of the primary carbides. At very low silicon concentrations, the primary carbides are elongated (Fig. 7.25a) and tend to become more equiaxed with increasing silicon concentration (considerable microscopy confirms that this is not just a sectioning effect). The changes imply that the orientation dependence of the liquid/M_7C_3 interface energy become less orientation dependent with increasing Si. A similar effect is evident for the eutectic M_7C_3 carbides which also appear more globular in alloy S3 (Fig. 7.25c). These morphological changes should be beneficial to the toughness of the alloy, perhaps imparting better impact abrasion wear resistance.
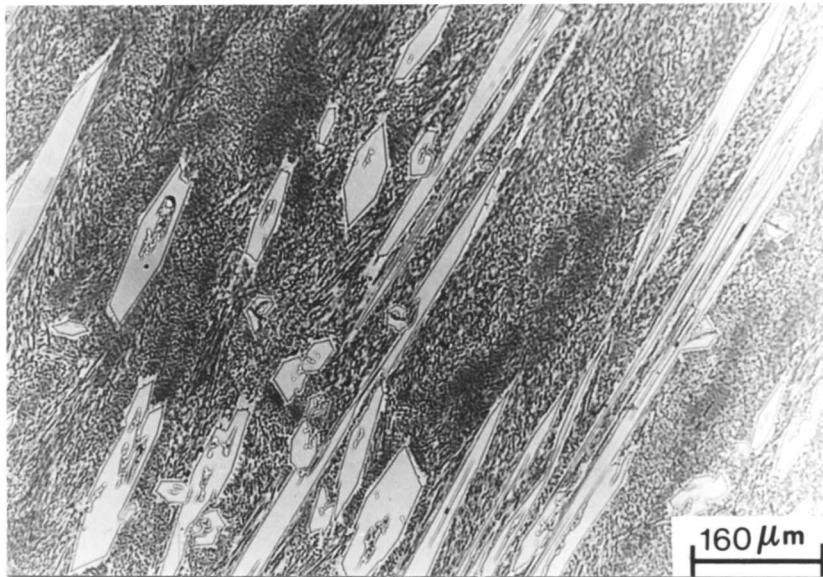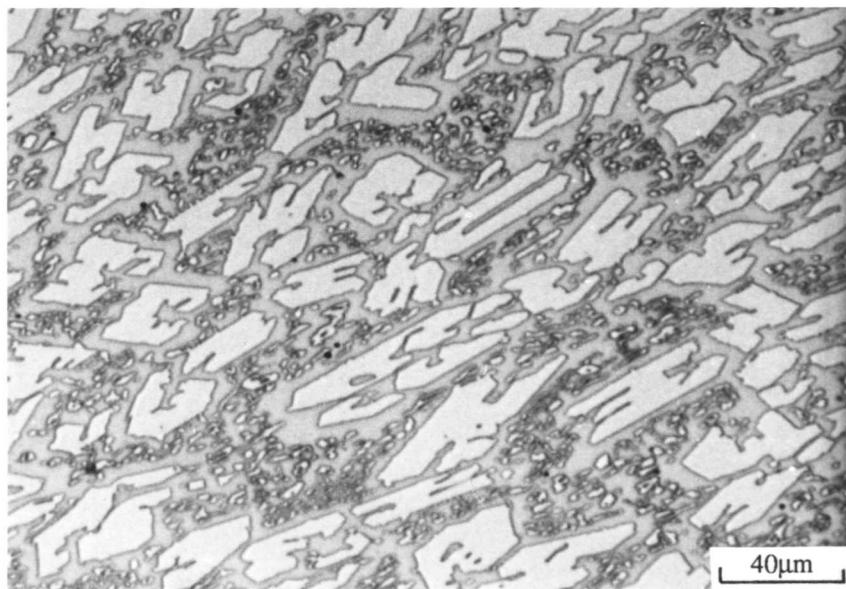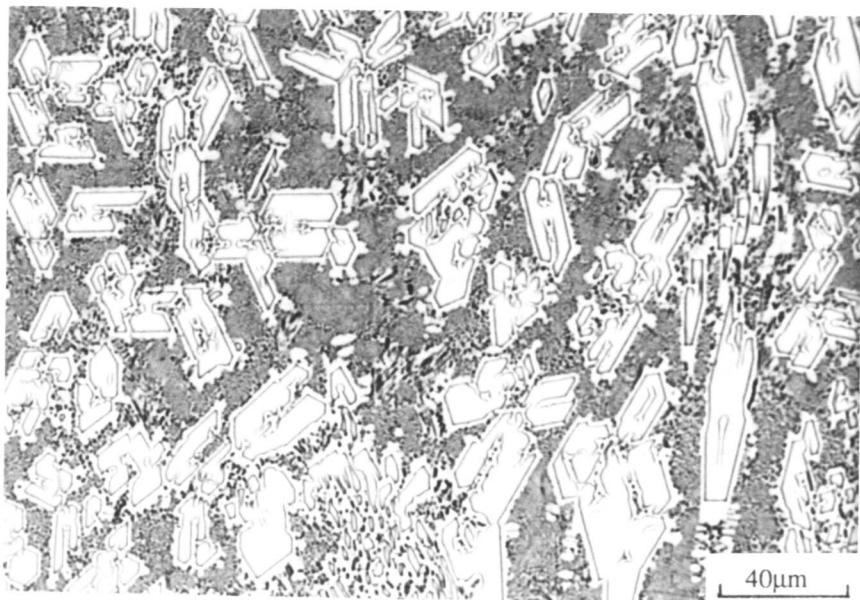
Fig. 7.25: Optical micrographs showing large primary M_7C_3 carbides in a eutectic mixture of matrix+M_7C_3. (a) Alloy S1; (b) Alloy S2; c) Alloy S3.
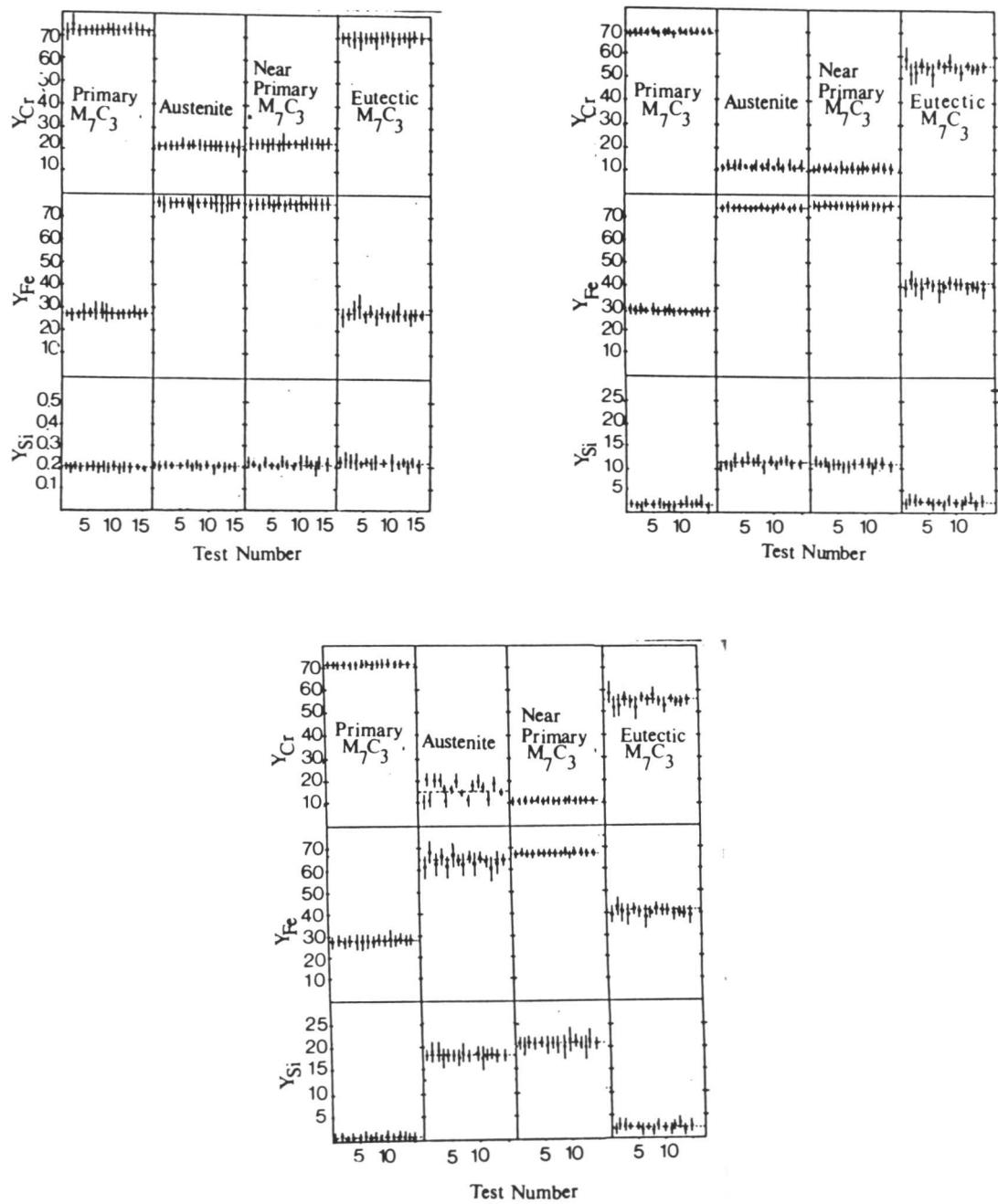
Fig. 7.26: Results of microanalysis experiments carried out in a transmission electron microscope. The dashed lines refer to the average composition. a) Alloy S1; b) Alloy S2; c) Alloy S3.

131

Table 7.9: Mean concentrations (atomic %) of the phases found in various alloys. The concentrations reported for regions near the primary M_7C_3 are probably unreliable due to some overlap of information from both primary M_7C_3 and matrix.

Alloy S1

	Primary M_7C_3	Near Primary M_7C_3	Matrix
Cr	50.8	22.9	20.9
Si	0.1	0.2	0.2
C	30	2.4	2.4

Alloy S2

	Primary M_7C_3	Near Primary M_7C_3	γ
Cr	48.9	11.5	11.5
Si	0.2	12.2	12.4
C	30	3.7	3.7

Alloy S3

	Primary M_7C_3	Near Primary M_7C_3	γ
Cr	50.5	10.9	14.3
Si	0.1	19.2	17.2
C	30	6.3	6.3

The microanalysis data (Fig. 7.26, Table 7.9) show that the silicon partitions strongly to the matrix. This should considerably enhance the oxidation and corrosion resistance of the alloys.

The effect of Si is also to reduce the level of Cr in the matrix during the eutectic decomposition of liquid. This may at first sight seem detrimental, but the austenite should in any case eventually decompose to low-chromium ferrite. The decrease in the Cr level of the matrix formed during solidification should in fact be beneficial since the Cr is best used in forming the hard M_7C_3 carbides during solidification.

The worn surfaces after the pin-on-disc abrasion tests show that carbides are effectively cut by the SiC and Al_2O_3 abrasives (Fig. 7.27).
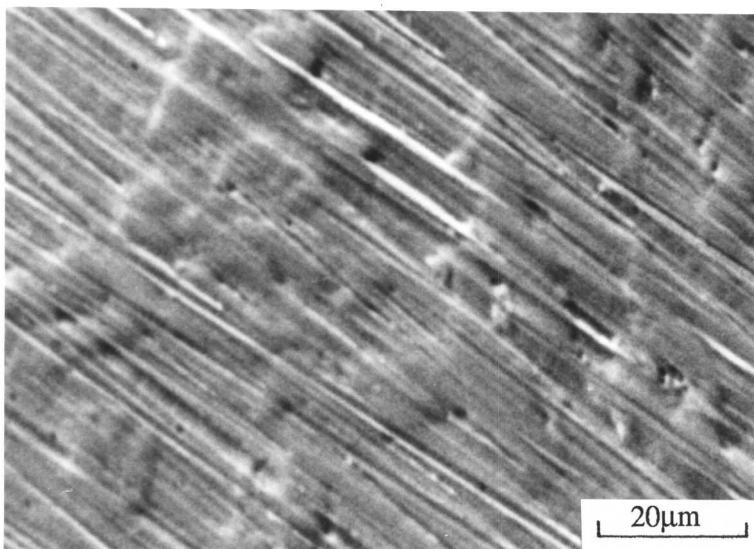
Fig. 7.27: Scanning electron micrograph of the worn surface of alloy S3 after the pin-on-disc abrasion test using SiC abrasives.

7.6.3 Conclusions

An attempt has been made to rationalise the influence of silicon on the detailed microstructure and phase composition of Fe-34Cr-4.5C alloys. The investigation has been carried out on model alloys cast by an argon arc melting technique, which is in general found to simulate adequately, the corresponding structures obtained by deposition during manual metal arc welding.

In all cases, Si is found to partition strongly into the matrix during solidification; Si concentrations of up to 18 at.% have been found in the matrix, even though the average Si concentration used was much lower.

It is found that Si causes significant changes in the morphology of M_7C_3 carbides. Both primary and eutectic M_7C_3 carbides tend to adopt more equiaxed morphologies and this has been attributed tentatively to Si causing a decrease in the orientation dependence of the liquid/M_7C_3 interfacial energy. In any case, the effect may be advantageous in enhancing the toughness, and hence, impact wear resistance of the high-Si alloys.

A further effect of Si is to reduce the Cr concentration of the matrix in the as-cast alloys. This is regarded as beneficial since the Cr is used better in the formation of M_7C_3 carbides, whose volume fraction should therefore increase with Si level. It is pointed out that if the austenite eventually decomposes to low-Cr ferrite, as required by equilibrium, then there is little point in having a high Cr content in the γ in any case.

133

7.7 Comparison of the Wear Resistance

In this study, Al_2O_3 and SiC abrasives were chosen in order to compare the effect of the hardness of abrasives at different applied loads and to examine material removal mechanisms under each abrasive. Pin-on-disc wear tests were performed in each sample using 450g and 1kg loads for Al_2O_3 and SiC abrasives respectively. Weight loss versus time curves of the abrasion test results with the Al_2O_3 abrasives for the alloys 78, T1, T2, and S3 are given in Fig. 7.28. The results show that alloy 78 has the lowest abrasive wear resistance among the four alloys. The worn surface of alloy 78 revealed extensive carbide cracking and spalling of the primary carbides (Fig. 7.9). Microanalysis experiments were carried out at the worn surface before the ultrasonic-cleaning so that fragments were identified. Some of the fragments were found to contain a great amount of Cr implying that these are Cr rich carbide fragments. It is well recognised that both plastic deformation and fracture mechanisms cause material removal of brittle solids during wear. However, material loss is an order of magnitude greater when fracture mechanisms are dominant. Therefore, the lowest wear resistance of Alloy 78 could be attributed to its highest volume fraction of carbides even though the material removal mechanism is the same as it is in the other alloys. Since primary carbides cannot firmly hold and resist being cut out by abrasives, the matrix will be vulnerable to fracture resulting in a higher weight loss. This conclusion is supported by the experimental results which show that Alloy T1 has a lower volume fraction of carbides than Alloys 78 and T1, subsequently better abrasive wear resistance. On the other hand, Alloy S3 was found to have the lowest weight loss even though its carbide volume fraction is higher than that of Alloys T1 and T2. This result is explained primarily by the different carbide morphology of the alloy S3. Strain energy, accompanied by the deformation, is released preferentially at the carbide/matrix interfaces due to high density of defects at these regions. This is consistent with the experimental observations which show extensive carbide cracking along the carbide/matrix interfaces. Therefore, it is feasible to suggest that carbides which have a more compact shape will be better supported by the matrix. Subsequently they will be less susceptible to interfacial cracking. The other advantage of the alloy S3 is that carbides are more closely spaced in this alloy so that they significantly support the matrix and reduce its ability to undergo plastic flow.

Similar experiments were carried out using the harder ($\approx$2480-2600 HV) SiC abrasive at 1kg load. The weight-loss time curves are given in Fig. 7.29. The results are found to be consistent with the above discussion. Apart from minor fluctuations, all the samples revealed an approximately constant wear rate indicating that strain hardening does not contribute to the wear resistance. Weight-loss was found to be higher for each sample compared to the Al_2O_3 abrasives. This is a reflection of a higher applied load and the higher hardness of the abrasives.
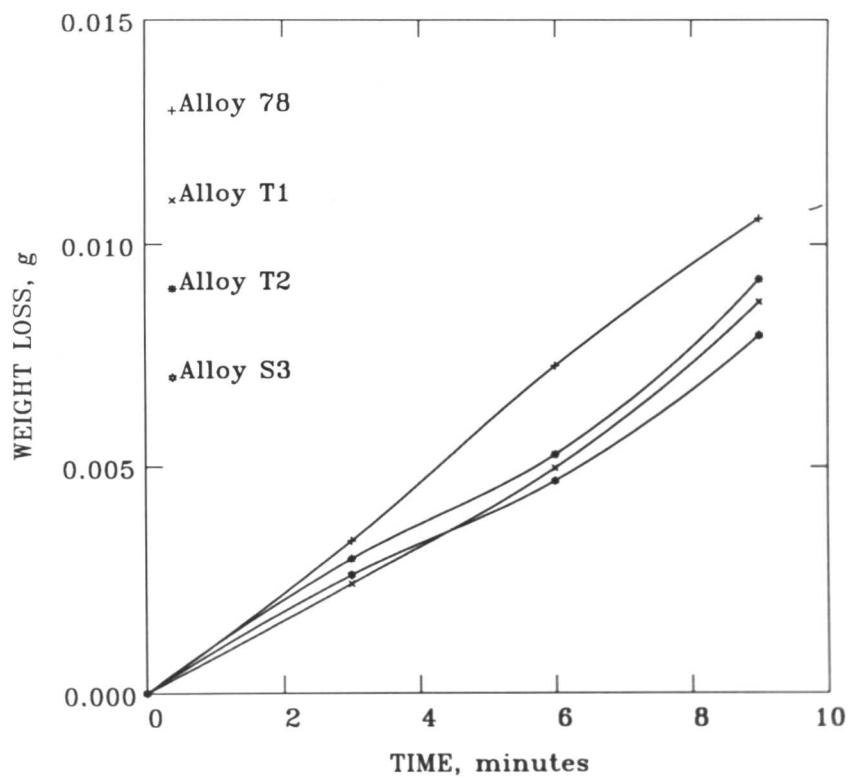
Fig. 7.28: Weight-loss time curves for the alloy 78, T1, T2, and S3 during pin-on-disc abrasion test using Al_2O_3 abrasives at 450g.
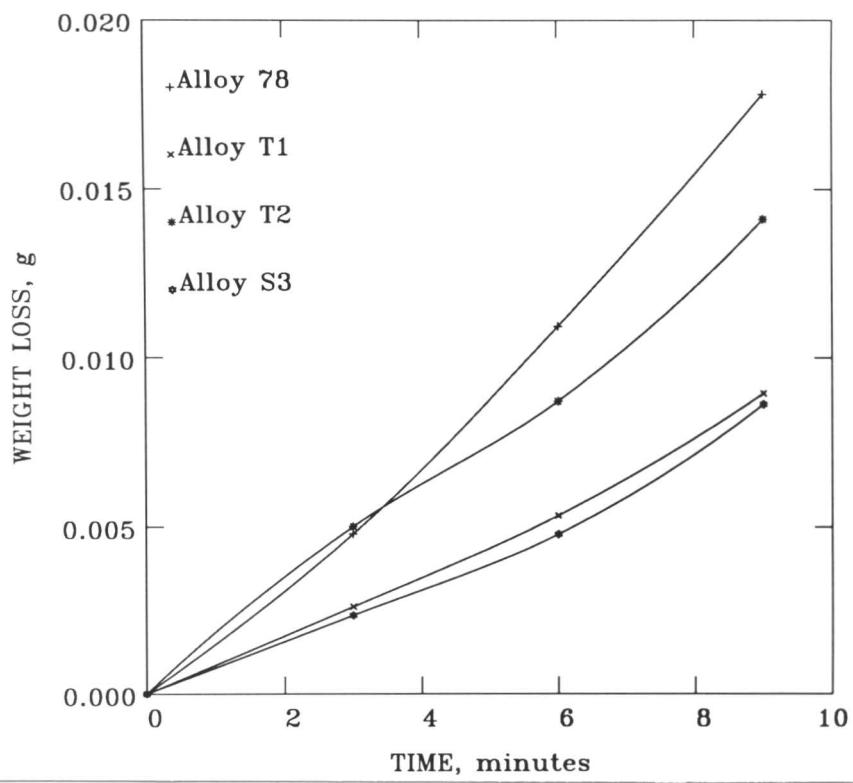

Fig. 7.29: Weight-loss time curves for the alloy 78, T1, T2, and S3 during pin-on-disc abrasion test using SiC abrasives at 1kg.

Scratch test experiments using the Vickers diamond reveal the considerable deformation of carbides in the form of cracks which are probably initiated at the carbide/matrix interfaces.

The results indicate that when the abrasives are hard enough to deform the carbides, they cause significant deformation, and spalling of the carbides giving rise to a high weight loss. In these conditions, although an increase of the carbide volume fraction is expected to lead to a greater chance of a lower wear resistance, the contribution of the carbide morphology and carbide spacing should be taken into account.

7.8 Thermodynamic Model

The condition for an alloy to be in equilibrium is that its Gibbs energy must be minimum. The most reliable method for calculating equilibrium compositions of phases is to minimize the Integral Gibbs Free Energy $(\Delta_f G)$[4] of mixing. Therefore, this model has been used in this study in order to calculate equilibrium mole fractions of each element in the Fe-Cr-C-M[5] system for the austenite/M_7C_3 equilibrium mixtures.

7.8.1 Computer Model for Minimization

The model presented here is based on standart methods available for the calculation of minimization with the help of the NAG Fortran Library.[31]

7.8.1.1 Geometric Representation and Terminology

The nature of the minimization problem in two dimensions is illustrated in Fig. 7.30, considering the following example

$$F(x) = e^{x_1} (4x_1^2 + 4x_2^2 + 4x_1x_2 + 2x_2 + 1) \qquad \dots(16)$$

The contours labelled $F_0, F_1, \dots$ in figure 1 are isovalue contours along which the function $F(x)$ takes specific constant values. The point x^* is a local unconstrained minimum at which the value of $F(x^*)$ is less than at all the neighbouring points. A function can have several such minima. Therefore, the lowest of the local minima has to be represented and termed a global minimum. For instance in the above figure x^* is the only local minimum. The point x is called a saddle point because it is a minimum along the line AB, but a maximum along CD. If the constraint $x_1 \geq 0$ is added to the minimizing of $F(x)$, the solution will not be altered. This constraint is represented by the straight line passing through $x_1 = 0$, and the hatching on this line represents the unacceptable region. The region R^n satisfies the constraints of the minimization problem and is termed the feasible region, and the point which satisfies the constraints is called a feasible point. If the nonlinear constraint (represented by the curved hatched line in figure 1) $x_1 + x_2 - x_1 x_2 - 1.5 \geq 0$ is added to the minimization, then x^* will not be a feasible point. In this new constrained problem the solution will be at point x which is the feasible point and corresponds to the smallest function value.

---

[4] The Integral Gibbs Free Energy $(\Delta_f G)$ of mixing is the difference between the molar Gibbs free energy $(G_m)^B$ for one mole of the phase B, and the Gibbs free energy of one mole of unmixed component, i.e. in the A-B system

$$\Delta_f G = G_m^B - [(1-x)^oG_A^{ref} + x\ ^oG_B^{ref}] \qquad \dots(15)$$

where x = mole fraction of component B, and $^oG_A\ ^oG_B$ are the Gibbs energy of pure A and B phases respectively.

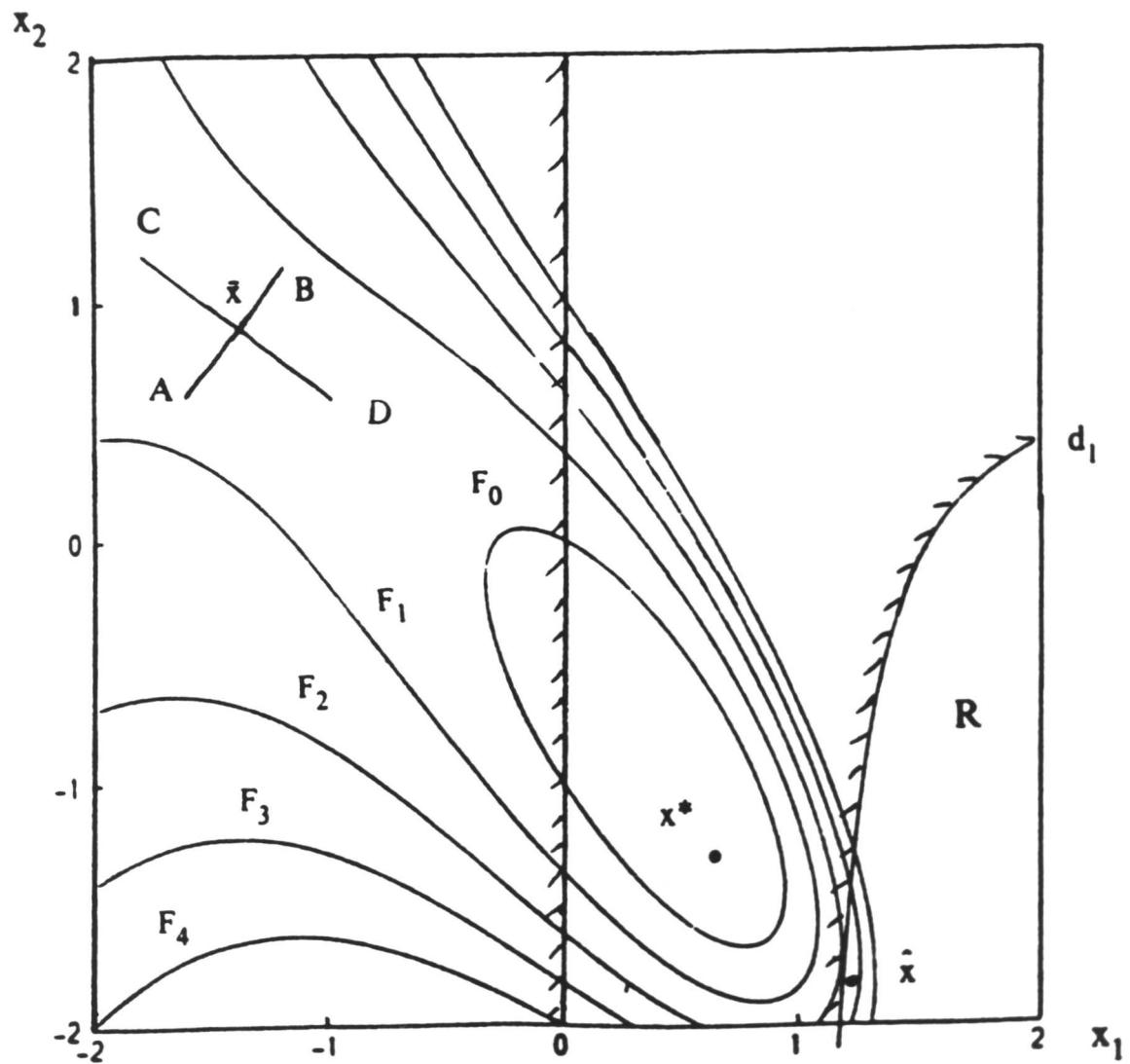[5] The M stands for the fourth alloying element (e.g. Ni, Mn, Si, Mo)

Fig. 7.30: Geometric representation of minimization.[31]

7.8.1.2 Gradient Vector

The vector of the first partial derivatives of F(x) is called the gradient vector, and is denoted by g(x)

$$g(x) = [\ \partial F(x)/\partial x_1,\ \partial F(x)/\partial x_2,..,\partial F(x)/\partial x_n]$$ .....(17)

The gradient vector has significance in minimization because it must be zero at an unconstrained minimum of any function with continuous first derivatives.

7.8.1.3 Hessian Matrix

The matrix of the second partial derivatives of a function is termed its Hessian matrix which is denoted by G(x), and its (i, j) (th) element is given by $\partial^2 F(x)/\partial x_i \partial x_j$. If F(x) has continuous second derivatives, the G(x) must be positive semi-definite at any unconstrained minimum of F.

7.8.1.4 Sufficient Conditions for a Solution of Minimization Subject to Bounds on the Variables

The minimization problem can be expressed mathematically as follows

minimize F(x),

subject to $l_i \leq x_i \leq u_i$ i=1,2,...,n

where l_i and u_i are lower and upper boundaries respectively for each variable.

This kind of expression assumes that upper and lower bounds exist on all the variables.

Sufficient conditions for a feasible point x^* at the solution of bounds-constrained problem are given as follows

(i) $g(x^*) = 0$

(ii) $G(x^*)$ is positive definite; and

(iii) $g_j(x^*) < 0$, $x_j=u_j$;

$\quad\quad g_j(x^*) > 0$, $x_j=l_j$;

where g(x) is the gradient of F(x) with respect to the free variables[6] and G(x) is the Hessian matrix of F(x) with respect to the free variables. The third condition ensures that F(x) cannot be reduced by moving off one or more of the bounds.

7.8.1.5 Quasi-Newton Method

The Quasi-Newton method approximates the Hessian $G(x^{(k)})$ by a matrix $B^{(k)}$ which is modified at each iteration, including information about the curvature of F along the latest search direction. It generates an iterative sequence $\{x^{(k)}\}$ that converges to the solution x^*.

The iteration sequence is generated as follows

$$x^{(k+1)} = x^{(k)} + \alpha^{(k)} p^{(k)}$$ .....(18)

where the vector $p^{(k)}$ is termed the direction of search, and $\alpha^{(k)}$ is the steplength which is

---

[6]

Variables which are not on their bounds are termed free variables.

chosen ensuring that $F(x)^{(k+1)} < F(x)^{(k)}$. The minimum of a function is found in n iterations.

7.8.2 Total Gibbs Free Energy and Variables

In a two phase system the total Gibbs free energy is given by

$$G^T = V_A G_A + (1-V_A)G_B$$

where G_A and G_B are the molar Gibbs free energies of the phases A and B respectively, and V_A is the mole fraction of phase A. This work aims to understand the effect of Ni, Mn, and Si on the equilibrium concentrations of alloying elements in the austenite or ferrite and M_7C_3 carbides. Therefore, the total Gibbs energy in this multicomponent system will be a function of each element and is represented as follows

$$G^T = V_{\alpha,\gamma}G^{\gamma/\alpha}(x_{Fe}^\gamma, x_{Cr}^\gamma, x_C^\gamma x_M^\gamma) + (1-V_{\alpha,\gamma})G^c(x_{Fe}^c, x_{Cr}^c, x_C^c, x_M^c) \qquad .....(19)$$

where

G^T is the total Gibbs free energy of the system,

$V_{\alpha,\gamma}$ is the mole fraction of austenite or ferrite,

$(1-\alpha)$ is the mole fraction M_7C_3 carbides,

$G^{\gamma/\alpha}$ is the Gibbs free energy of the formation of austenite or ferrite,

G^c is the Gibbs free energy of M_7C_3 carbides,

x_{Fe}^γ is the mole fraction of Fe in austenite or ferrite,

x_{Cr}^γ is the mole fraction of Cr in austenite or ferrite,

x_C^γ is the mole fraction of C in austenite or ferrite,

x_M^γ is the mole fraction of M (th) element in austenite or ferrite,

x_{Fe}^c is the mole fraction of Fe in the M_7C_3,

x_{Cr}^c is the mole fraction of Cr in the M_7C_3,

x_C^c is the mole fraction of C in the M_7C_3,

x_M^c is the mole fraction of M (th) element in M_7C_3.

Since the total mole fraction of each phase is equal to 1, the number of unknowns could be directly reduced to seven from nine as follows

$$x_M^\gamma = 1 - x_{Fe}^\gamma - x_{Cr}^\gamma - x_C^\gamma \qquad .....(20)$$
$$x_M^c = 1 - x_{Fe}^c - x_{Cr}^c - x_C^c \qquad .....(21)$$

The mole fraction of carbon in M_7C_3 is equal to 0.3 assuming stoichiometry. Furthermore, two more unknowns could be represented by the others using the following mass-balance equations

$$x_{Fe}^T = x_{Fe}^\gamma \alpha + x_{Fe}^c(1-\alpha) \qquad .....(22)$$
$$x_{Cr}^T = x_{Cr}^\gamma \alpha + x_{Cr}^c(1-\alpha) \qquad .....(23)$$
$$x_M^T = x_M^\gamma \alpha + x_M^c(1-\alpha) \qquad .....(24)$$

140

where x_{Fe}^T, x_{Cr}^T, and x_M^T are the mole fractions of total Fe, Cr, and M (Ni, Mn, Si) in the alloy. The mole fraction of austenite or ferrite could be written using one of the above mass-balance equations as follows

$$V_\gamma = (x_{Fe}^T - x_{Fe}^c) / (x_{Fe}^{\gamma,\alpha} - x_{Fe}^c) \qquad .....(25)$$

x_{Cr}^c and x_M^c could be represented by the other unknowns using the equations 20-23.

$$x_{Cr}^c = (x_{Cr}^T (x_{Fe}^\gamma - x_{Fe}^c) - x_{Cr}^\gamma (x_{Fe}^T - x_{Fe}^c)) / (x_{Fe}^\gamma - x_{Fe}^T) \qquad .....(26)$$

$$x_M^c = x_M^T (x_{Fe}^\gamma - x_{Fe}^c) - x_M^\gamma (x_{Fe}^T - x_{Fe}^c)) / (x_{Fe}^\gamma - x_{Fe}^T) \qquad .....(27)$$

Finally, minimization of the total Gibbs free energy of the system can be calculated considering only four unknowns (x_{Fe}^γ, x_{Cr}^γ, x_C^γ, and x_{Fe}^c). A schematic example representing the minimization of the total Gibbs free energy in two phase system is illustrated in Fig. 7.31.
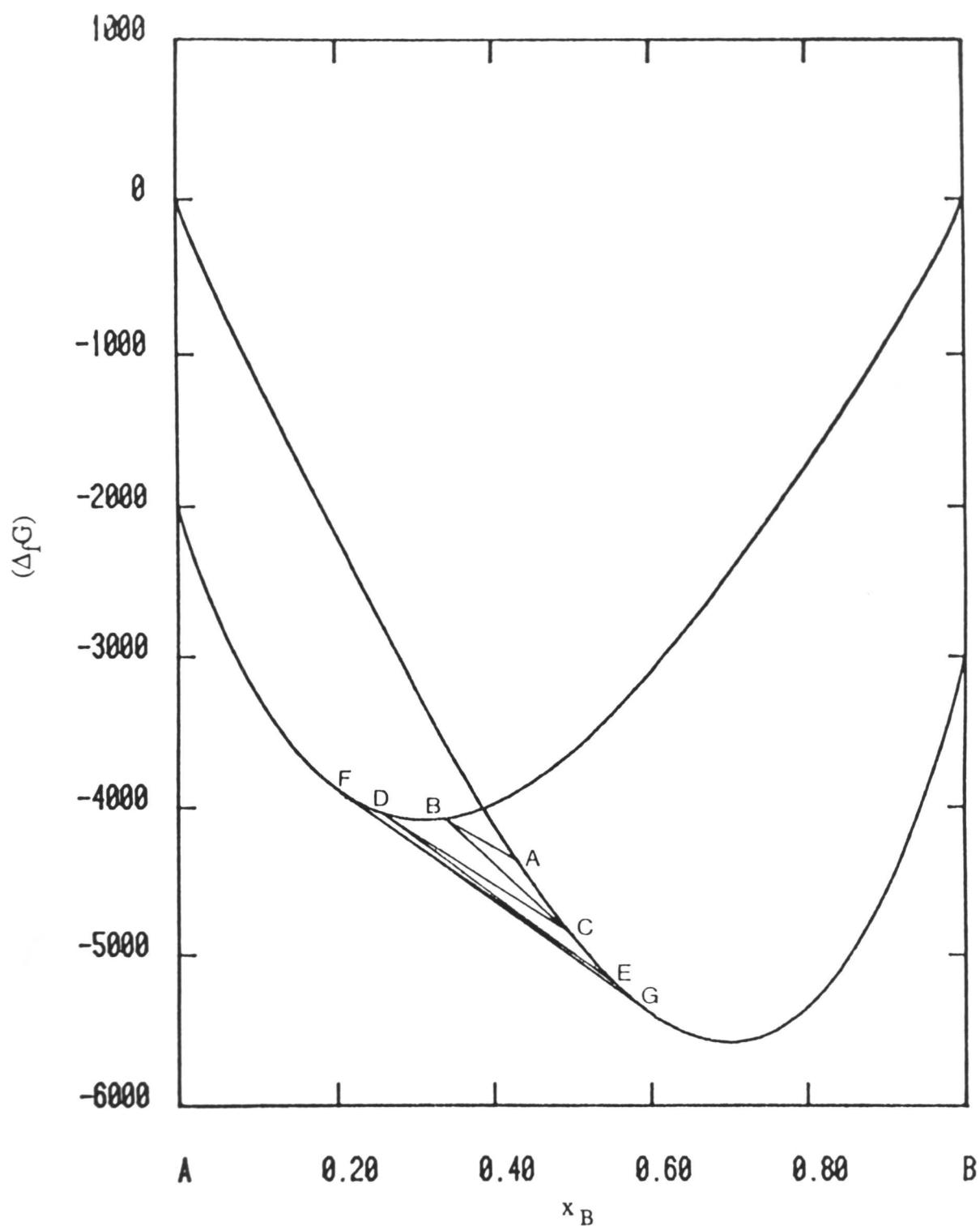
Fig. 7.31: Application of the Quasi-Newton model for finding the minimum Gibbs free energy of the system containing two solution phases.[32]

In Fig. 7.31 $\Delta_f G$ is the integral Gibbs free energy of mixing and x_B is the mole fraction of phase B. The first guess values are used to construct the line A-B for a given alloy composition x_0. Since G_m has to be a minimum in equilibrium ($\Delta_f G$ has its least possible value) p must be at the lowest possible point. The line A-B is later modified until the feasible point is reached. Subsequently, the line H-I is found to be representing the common-tangent line which determines the equilibrium compositions (x^α, x^γ).

The model which was originally suggested by Hillert and Staffanson,[33] and later modified for quaternary system by Harvig[34] is used in this study. This model was developed for ionic melts and interstitial solutions and based upon the use of atomic ratios rather than atom fractions. The concentration of an interstially dissolved element is expressed by the fraction of interstitial sites occupied by that element. For instance, ferrite has three interstitial sites for carbon per metal atom whereas austenite has only one.

$$c/a=1 \text{ for austenite, } c/a=3 \text{ for ferrite}$$

where a is the number of metal atoms per mole, and c is the corresponding number of interstitial sites which are available. The molar ratios are defined as follows

$$y_M = x_M / (1-x_C) \qquad .....(28)$$
$$y_C = a/c \; x_C / (1-x_C) \qquad .....(29)$$

where M stands for metal (in this work M refers to the Fe, Cr, and fourth alloying element e.g., Ni, Mn, Si). This model has been used successfully for solutions containing one interstitial and one or two substitutional solutes and was later modified for quaternary systems by Harvig.[34] The Gibbs energy per mole of metal atoms for austenite and ferrite is represented as follows

$$
\begin{aligned}
G_m =\; & y_{Fe}{}^{\circ}G_{Fe} + \sum_M y_M{}^{\circ}G_M + y_C({}^{\circ}G_{FeC_c} - {}^{\circ}G_{Fe} \\
& + RT\,[y_{Fe}\ln y_{Fe} + \sum_M y_M \ln y_M + c y_C \ln y_C \\
& + c(1-y_C)\ln(1-y_C)] + y_C \sum_M y_M \Delta G_M \\
& + y_{Fe}\sum_M y_M[y_C L^C_{FeM} + (1-v)L^v_{FeM}] + y_C(1-y_C[y_{Fe}L^{Fe}_{Cv} \\
& + \sum_M y_M L^M_{Cv}]
\end{aligned}
\qquad .....(30)
$$

where M stands for Cr and the fourth alloying element. ΔG_M represents the difference between four standard states and is given by

$$\Delta G_M = {}^{O}G_{Fe} + {}^{O}G_{MC_c} - {}^{O}G_M - {}^{O}G_{FeC_c} \qquad .....(31)$$

This parameter is also the major parameter expressing the Cr-C interaction in austenite and ferrite. L parameters are interaction parameters. For example, $L_{CV}{}^{Fe\gamma}$ describes the interaction between carbon and vacant interstitial sites when the metal lattice is completely filled with iron atoms in the austenite. ${}^{O}G_{Fe}$ and ${}^{O}G_M$ are the molar Gibbs energies of pure elements in the same state as the solution under consideration. ${}^{O}G_{FeC}$ and ${}^{O}G_{CrC}$ are the molar Gibbs energies of

hypothetical cases assuming that all the interstitial sites are occupied by carbon atoms.

The Gibbs energy of the carbides was described by Nishizawa and Uhrenius[35] and the same model will be accepted in this present work. The following equation expresses the Gibbs energy per mole of metal atoms for carbides

$$G_m = y_{Fe}{}^\circ G_{FeCb} + \sum_M y_M{}^\circ G_{MCb} + RT[y_{Fe} \ln y_{Fe}$$
$$+ \sum_M y_M \ln y_M] + y_{Fe} \sum_M y_M A_{FeM} + \frac{1}{2} \sum_M \sum_{N \neq M} y_M y_N A_{MN} \qquad .....(32)$$

where b is written for a stoichiometric compound M_aC_c as b=c/a. $^OG_{FeC_b}$ and $^OG_{MC_b}$ are the Gibbs energies of formation per mole of Fe_aC_c and M_aC_c respectively, referring to the elements in the same structural state. A is the interaction parameter (e.g. A_{FeCr} describes the interaction parameter between Fe and Cr in carbide).

7.8.3 Results and Discussion

The effect of Si, Mn and Ni on the equilibrium mole fractions of each element in the Fe-Cr-C-M system has been studied. Fe-30Cr-4.5C (wt%) alloy was chosen as a reference alloy and the results were compared at 1273K. Fig. 7.32 represents the effect of Si on the mole fraction of Cr in the austenite. The results are found to be consistent with the experimental observations showing that an increase of Si content in the reference alloy leads to a significant decrease of Cr concentration in the austenitic matrix. This may seem to be detrimental to oxidation and corrosion resistance but as discussed earlier in any case austenite transforms to low chromium (≈3wt%) ferrite. Furthermore, calculations show that Si is rejected by the carbides resulting in a matrix with 18at% Si in the 7wt%Si containing alloy. This result has significant consequences since it is well recognized that Si greatly improves the oxidation and corrosion resistance by forming silicon oxides. The other advantage of the Si addition is that it increases volume fraction of M_7C_3 carbides. As it is illustrated in Fig. 7.32 the volume fraction of carbides increases from about ≈0.54 to ≈0.68 when the Si content increased to 7wt% in the reference alloy. Since an increase in carbide volume fraction generally leads to an increase of abrasion resistance (particularly low-stress abrasion), Si addition has also a beneficial influence in abrasion resistance.

In contrast, Mn and Ni additions increased Cr concentration in the matrix and subsequently decreased the volume fraction of M_7C_3 carbides (Fig. 7.33). This decrease could probably be detrimental for abrasion resistance particularly when the abrasives are not hard enough to deform the carbides.

144
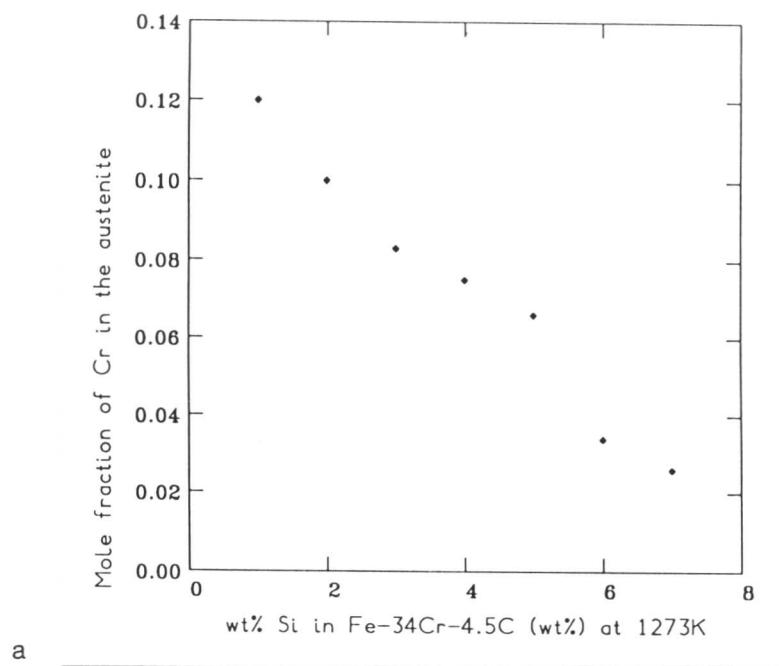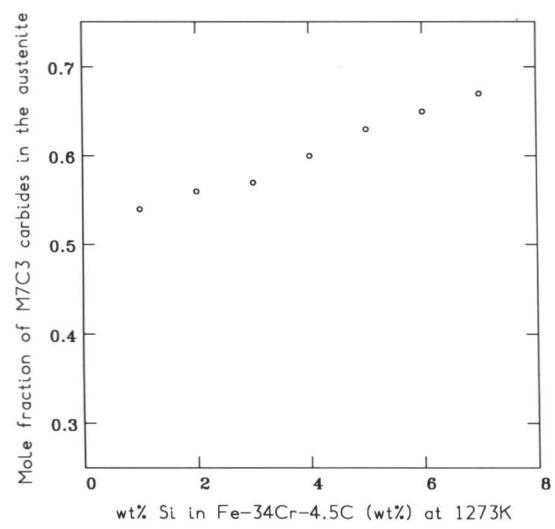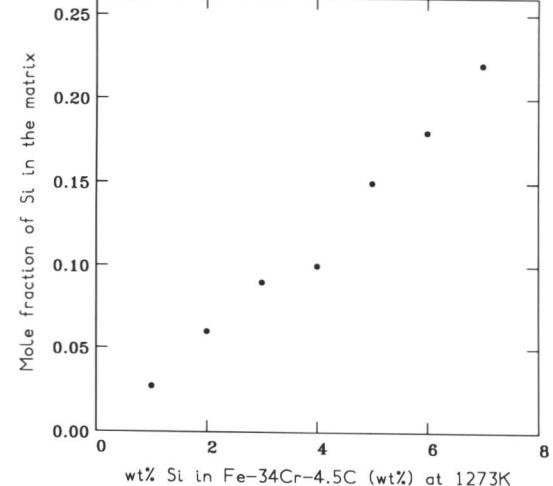
Fig. 7.32: Effect of Si (wt%) in Fe-30Cr-4.5C (wt%) alloy at 1273K on a) mole fraction of Cr in the austenite (y_{Cr}^{γ}); b) M_7C_3 carbide volume fraction; c) mole fraction of Si in the austenite (y_{Si}^{γ}).

145
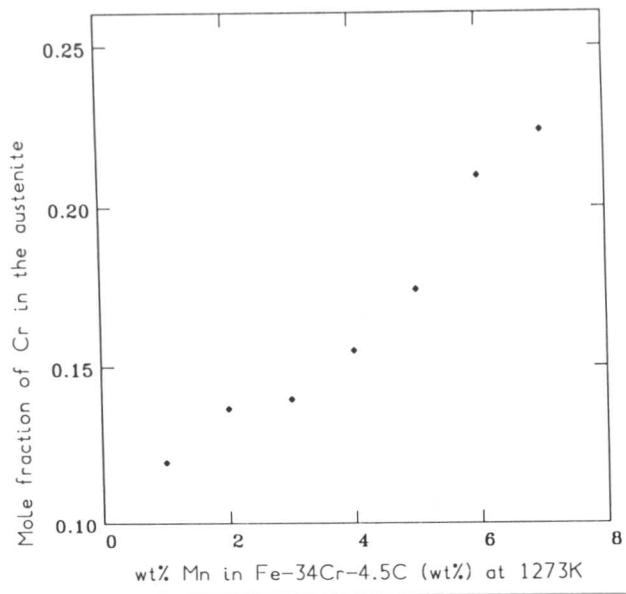
a
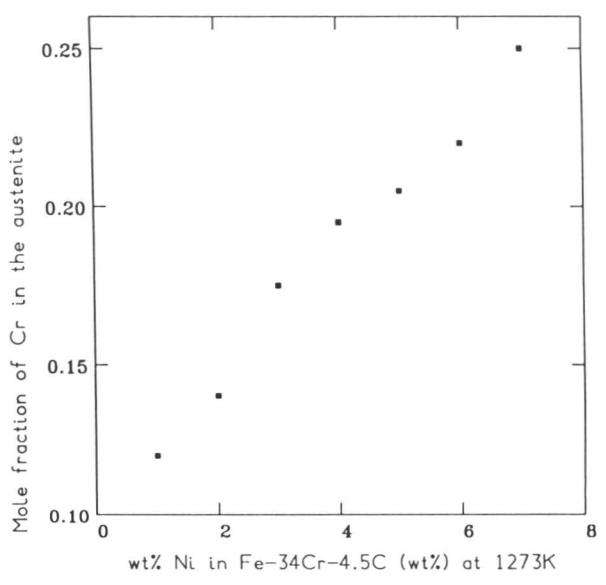
b
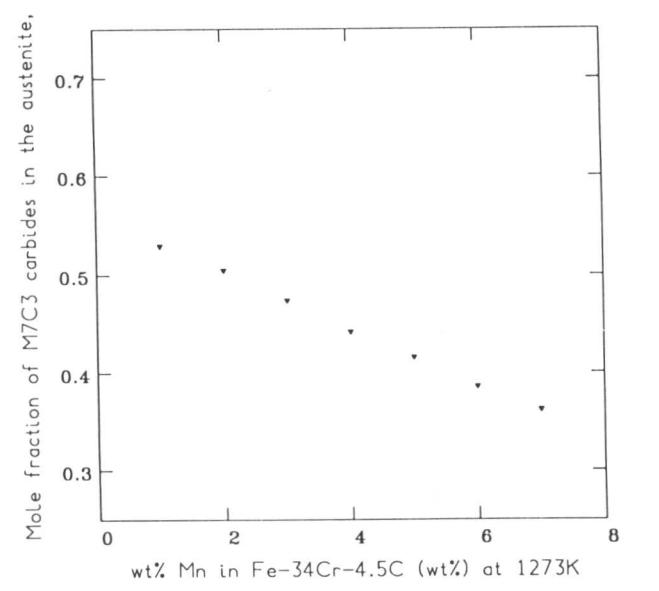
c

d

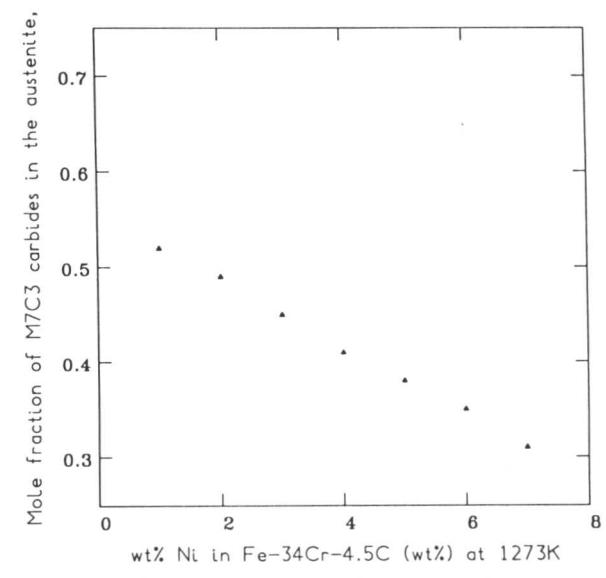Fig. 7.33: Effect of Mn, and Ni (wt%) in Fe-30Cr-4.5C (wt%) alloy at 1273K on a) effect of Mn on the mole fraction of Cr in the austenite (y_{Cr}^{γ}); b) effect of Ni on the mole fraction of Cr in the austenite (y_{Cr}^{γ}); c) effect of Mn on the M_7C_3 carbide volume fraction; d) effect of Ni on the M_7C_3 carbide volume fraction.

7.8.4 Conclusions

The minimization of the total Gibbs free energy method is used to calculate the equilibrium mole fractions of each element in the Fe-Cr-C-M system (where M refers to the Si, Mn, and Ni) when the austenite is in equilibrium with M_7C_3. The total Gibbs free energy of the quaternary system is minimized using the Quasi-Newton method which minimizes the function in n iterations. The thermodynamic model was developed for ionic melts and interstitial solutions that were based on the use of atomic ratios rather than atom fractions.

The results showed that Mn and Ni additions increased the mole fraction of Cr in the austenite, and decrease the volume fraction of M_7C_3 carbides. In contrast, the Si addition decreased the Cr concentration of the austenitic matrix resulting in a Si enriched matrix and high volume fraction of M_7C_3 carbides (≈ 0.7). The results are found to be reasonably consistent with the experimental observations.

147

7.9 References

1) D. DYSON, and B. HOLMES: J. of the Iron and Steel Institute: 1970, 469.
2) L. SVENSSON, B. GRETOFT, B. ULANDER, AND H. K. D. H. BHADESHIA: J. Mat. Sci., 1986, **21**, 1015.
3) A. P. MERCER: 'The effects of atmospheric humidity and oxygen on the wear of metals by fine abrasives', Ph.D. Thesis, October 1985, University of Cambridge.
4) Diffusion and Defect Data: Ed. F. H. WOHLBIER, Materials Review Series, 1976.
5) K. EASTERLING: "Introduction to the Physical Metallurgy of Welding", 1983.
6) Metals Handbook, 1973, ASM, USA, 402.
7) D. TURNBULL: Metall. Trans. A, 1981, **12A**, 695.
8) B. UHRENIUS: "Hardenability Concepts with Applications to Steel", Eds. D. V. DOANE, and J. J. KIRKALDY, Met. Soc. AIME, USA, 1977, 28.
9) R. E. SCHRAMM, and R. P. REED: Metall. Trans. A, 1975, **6A**, 1345.
10) M. J. JOHNSON, and P. J. PAVLIK: 'Atmospheric Corrosion of Stainless Steels', in Proc. Conf. 'Atmospheric Corrosion', Ed. W. H. AILOR, 1982,4
11) K. H. ZUM GAHR: Z. Metalkde, 1980, **71**, 103.
12) H. K. D. H. BHADESHIA: in Proc. Conf. 'Solid-Solid Phase Transformations August 10-14 1981, Metallurgical Society of AIME, 1041.
13) V. M. ERSHOV: Steel in the USSR: 1984, **8**, 101.
14) K. C. THOMPSON, and J. W. EDINGTON: "Practical Electron Microscopy in Materials Science", Monograph 2, 1977.
15) J. W. MARTIN, and R. D. HONERTY: "Stability of Microstructure in Metallic Systems", Cambridge University Press, 1976.
16) M. Y. WEY, T. SAKUMA, and T. NISHIZAWA: Trans. of the Japan Institute of Metals, 1981, **22**, 733.
17) A. W. BOWEN, and G. M. LEAK: Metall. Trans. A, 1970, **1A**, 1695.
18) Metals Handbook, 9th edition, ASM, Ohio, USA, 1983, **6**, 771.
19) Welding Handbook, Ed. W. H. KEARNS, American Welding Society, 7th edition, **2**, 1978.
20) U. R. LENEL, and B. R. KNOTT: In Proc. Conf. 'Wear of Materials 87', New York, 1987, Am. Soc. Mech. Eng., 635.
21) S. SHEPPERSON, and C. ALLEN: In Proc. Conf. 'Wear of Materials 87', New York, 1987, Am. Soc. Mech. Eng., 573.
22) A. M.EL-RAKAYBY, and B. MILLS: Wear, 1986, **112**, 327.
23) W. C. HAGEL, and E. K. OHRINER: Molybdenum Mosaic, **6**, 12.
24) C. McCAUL, and S. GOLDSPIEL: in the Corrosion Monograph Series 'Atmospheric Corrosion', Ed. W. H. AILOR, The Electrochemical Society, Princeton, New Jersy, 1982, 430.
25) P. F. WIESER: in the Corrosion Monograph Series 'Atmospheric Corrosion', Ed. W. H. AILOR, The Electrochemical Society, Princeton, New Jersy, 1982, 453.
26) S. ATAMERT, and H. K. D. H. BHADESHIA:in Proc. Conf. 'Heat Treatment 87' London, May 1987, The Institute of Metals.
27) W. S. OWEN: Trans. ASM, 1954, **46**, 812.
28) S. ATAMERT: C.P.G.S Thesis, 1986, University of Cambridge.
29) N. BIRICS, and G. H. MEIER: "Introduction to High Temperature Oxidation of Metals", London, 1983, 85.
30) S. MALM: Scand. J. Metallurgy, 1976, **5**, 137.
31) NAG (National Algorithms Group) Ltd., Fortran Library Manual, Oxford, U.K.
32) A. T. DINSDALE: 'The Generation and Application of Metallurgical Thermodynamic Data', NPL Report DMA (C) 25, August 1984.
33) M. HILLERT, and L.-I. STAFFANSSON: Acta Chem. Scand., 1970, **24**, 3618.
34) H. HARVIG: Acta Chem. Scand., 1971, **25**, 3199.
35) T. NISHIZAWA, and B. UHRENIUS: Scand. J. Metallurgy, 1977, **6**, 67.

8. EFFECT OF THE CARBIDE FORMING ELEMENTS Nb, Ti, Mo, V, AND W ON THE MICROSTRUCTURE AND ABRASIVE WEAR RESISTANCE

8.1 Effect of Nb and Ti on the Microstructure and Abrasive Wear Resistance

8.1.1 Introduction

Nb and Ti are often added to Fe-Cr-C alloys in order to obtain very hard MC (TiC, NbC) type carbides.[1-9] These hard primary carbides (NbC=2300 HV, TiC=2900 HV[10]) are not easily scratched by natural minerals. If there is uniform distribution of these carbides, and if they are closely spaced, abrasives cannot effectively penetrate into the matrix phase, leading to higher wear resistance. The abrasive wear resistance of NbC and TiC containing alloys has been found to be better than that of M_7C_3 carbide containing alloys.[11] This has been attributed to the high hardness and uniform distribution of these carbides. Even though there is a considerable amount of experimental evidence for the beneficial effect of NbC and TiC, no systematic research has been carried out towards their microstructural control.

8.1.2 Experimental Techniques

Alloy 79 (Fe-23.11Cr-3.57C-9.38Nb-1.29Si-0.42Mn-0.036P wt%) was deposited by the manual metal arc (MMA) welding technique. The welding conditions were 200A, 23V with a deposition rate of about 0.004m/s. The interpass temperature was 500°C. The weld deposit consisted of three layers so that the top layer microstructure was essentially undiluted by the mild steel substrate.

Alloy H3 (Fe-31.5Cr-3.69C-7.20Ti-1.0Mo-0.32Ni-0.27Si wt%) was cast by an argon arc melting technique.

Microanalysis experiments were carried out using scanning electron microscope as outlined in Chapter 10. The pin-on-disc abrasion tests were carried out using SiC abrasives (180 mesh) at a 2kg applied load on 3mm diameter specimens. The Vickers diamond was used for single-pass scratch test experiments under 500g and 1000g applied loads. The worn surfaces were ultrasonically cleaned and examined in a scanning electron microscope.

8.1.3 Results and Discussion

If the effect of Nb and Ti is ignored, one would expect the solidification sequence of the Alloy 79 and H3 to be the same as in Alloy 78. However, since Nb and Ti are very strong carbide forming elements, they form primary MC (TiC, NbC) type carbides as the first solid phase during cooling. In addition, the microstructure also contains austenite dendrites with interdendritic M_7C_3 carbides (Figs. 8.1a,b). Nb and Ti tie up a high amount of C and reduce the amount of M_7C_3. The presence of NbC and TiC has been reported to be more effective in increasing abrasive wear resistance than either raising the eutectic M_7C_3 content, or increasing

the width of the M_7C_3 eutectic carbide particles.[3] If, however, the MC carbides are not uniformly distributed and finely spaced, abrasive particles easily penetrate into the matrix phase, due to the relatively small size of the MC carbides when compared with the large primary M_7C_3 particles of the type found in Alloy 78.

Microanalysis results (Figs. 8.2 and 8.3, and Tables 8.1 and 8.2) showed that the matrix contained only small amounts of Nb, and Ti. The Cr concentration of the austenitic matrix of Alloy H3 was found to be higher than that of the Alloy 79, consistent with the higher Cr concentration in the former alloy.

Scanning electron micrographs of the worn surfaces after the pin-on-disc test using SiC abrasive paper showed that NbC are cut by the abrasives, but to a lesser extent than the eutectic areas (Fig. 8.4a,b). Furthermore, NbC particles were found to protrude from the surface, and the scratch grooves decreased in width as they crossed the NbC particles (Fig. 8.4b).

In the Ti containing alloy, worn surface analysis suggested that TiC particles are occasionally cut and broken (Fig. 8.5).

The single-pass scratch tests revealed that the eutectic regions are ploughed into both edges of the scratch groove (Figs. 8.6a,b). Primary carbide cracking was also observed with two different loads (500g and 1000g), the cracking becoming more apparent at 1kg load. Micromachining chips in the eutectic areas suggest that those regions are easily deformed, and consequently provide inefficient support to the primary MC carbides.
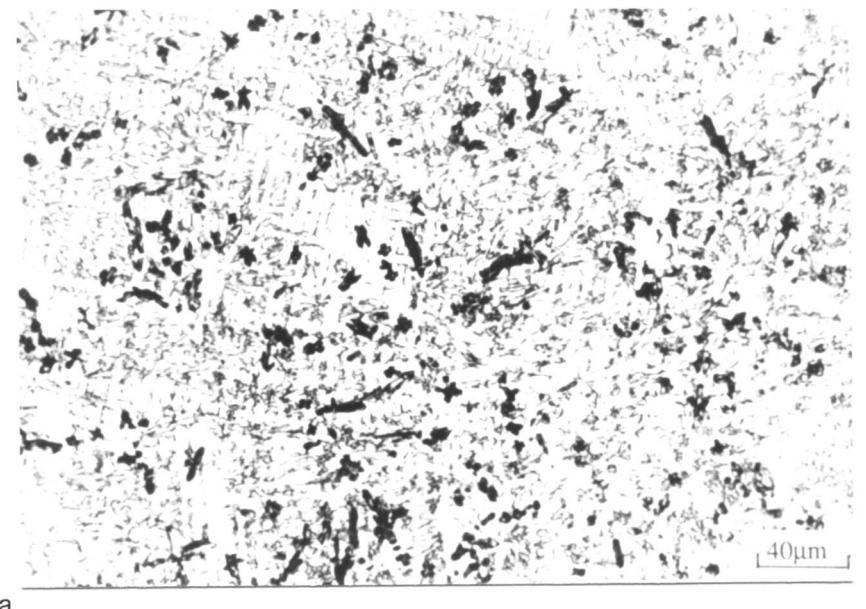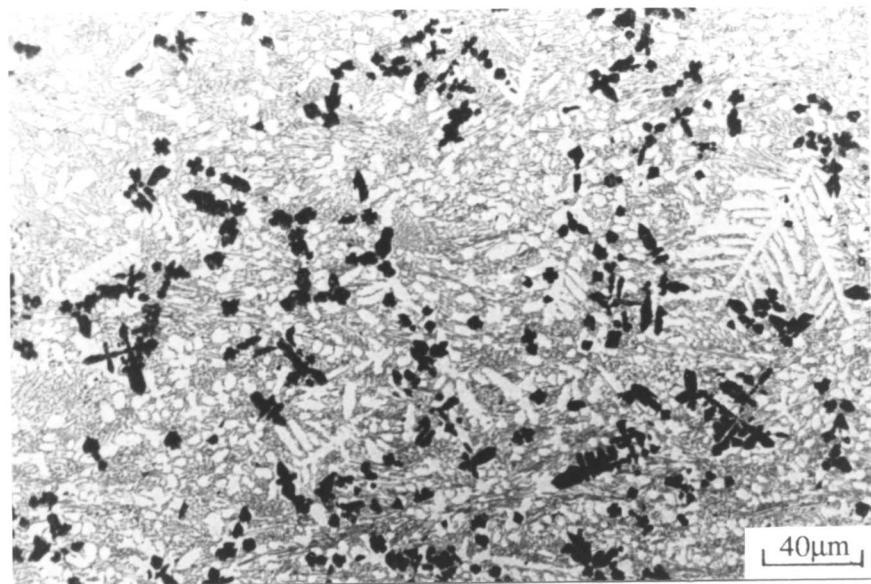
Fig. 8.1: a) Optical micrograph of the top layer of Alloy 79 consisting of primary NbC (black particles), and eutectic M_7C_3 carbides (grey particles) with pro-eutectic austenite dendrites; b) optical micograph of Alloy H3 consisting of uniformly distributed TiC (black particles) and M_7C_3 eutectic carbides and pro-eutectic austenite dendrites.
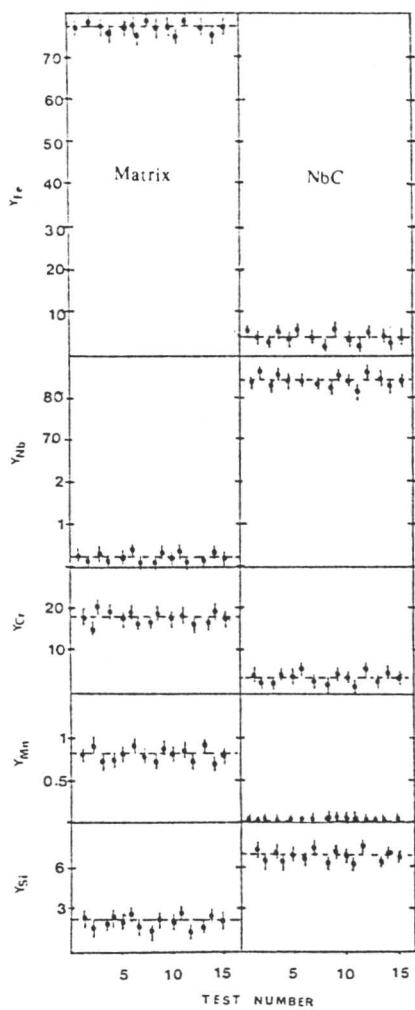
Fig. 8.2: Microanalytical data from Alloy 79 at%. The continuous lines show the average concentrations in each phase. The experiments were carried out using a scanning electron microscopy and energy-dispersive X-ray analysis.

Table 8.1: Mean compositions of phases of Alloy 79 (at%). The results are quoted to three decimal places for internal consistency.

	Matrix	NbC
Fe	77.990	4.514
Cr	18.090	3.420
Nb	0.252	84.290
Mn	0.786	0.043
Si	2.857	6.980
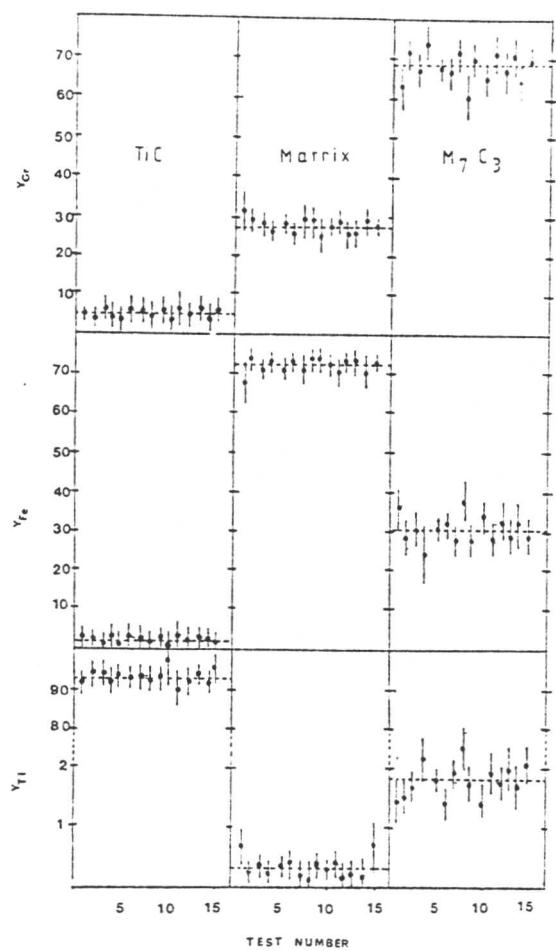
Fig. 8.3: Microanalytical data from Alloy H3 at%. The continuous lines show the average concentrations in each phase. The experiments were carried out using a scanning electron microscopy and energy-dispersive X-ray analysis.

Table 8.2: Mean compositions of the phases of Alloy H3. The results are quoted to three decimal places for internal consistency.

	Ti Carbide		Austenite		Eutectic Carbide	
	Y_i	V_i	Y_i	V_i	Y_i	V_i
Fe	1.930	0.965	72.018	71.023	30.056	21.047
Cr	4.400	2.201	27.656	27.270	68.113	47.690
Ti	92.984	46.492	0.326	0.321	1.831	1.282
C		50		1.394		30

153

a

b
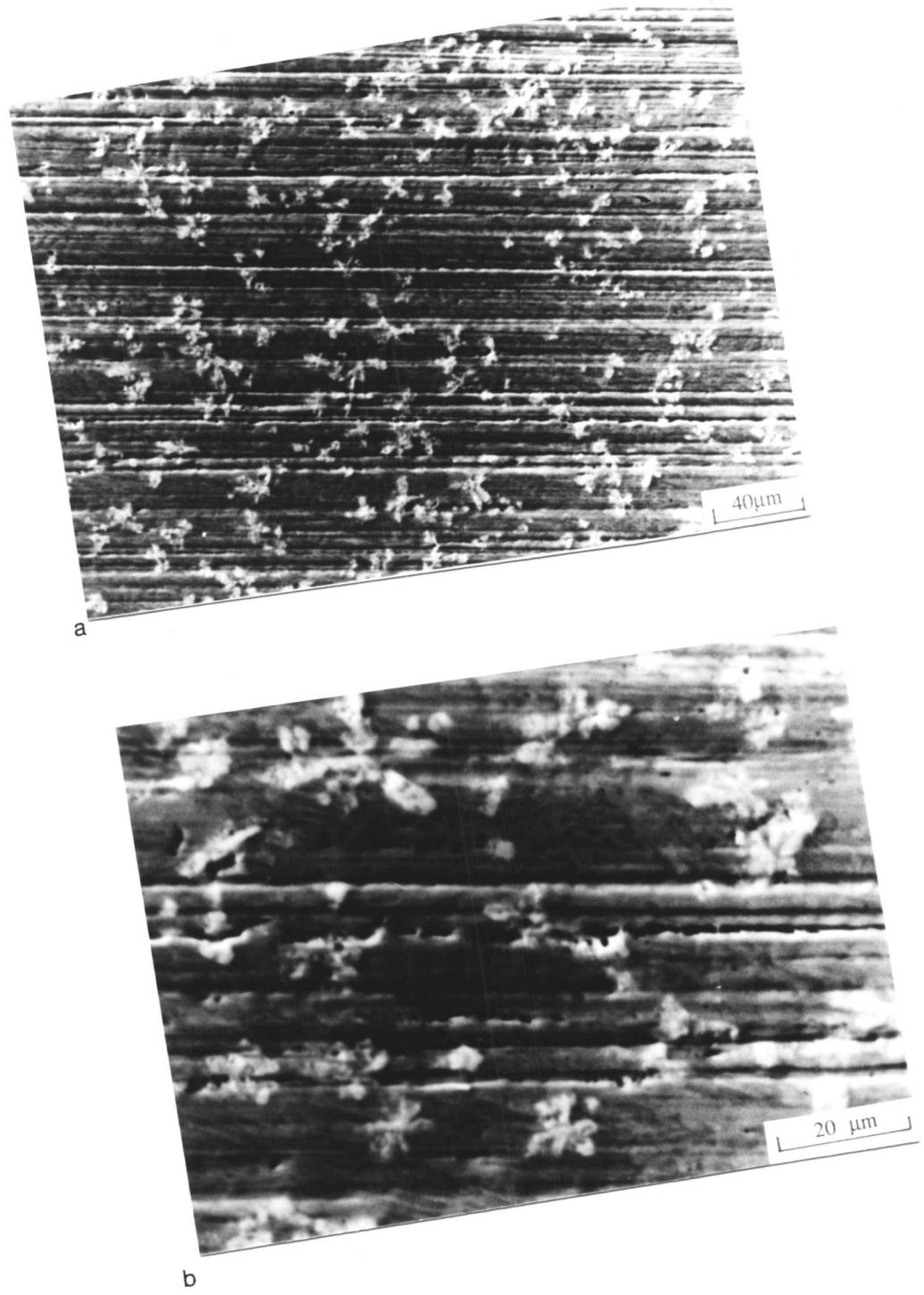
Fig. 8.4:   Scanning electron micrographs of the worn surfaces of Alloy 79 after pin-on-di abrasion tests using SiC (180 mesh) abrasives and a 2kg load. a) low magnification; b) hi magnification. It is clear that the abrasives are able to cut the NbC particles. Nonetheless, scratch groove width in NbC is seen to be narrower than in the eutectic areas suggesting that primary NbC improve wear resistance.

Fig. 8.5:   Scanning electron micrograph of the worn surface of Alloy H3, after the pin-on-disc abrasion test using SiC (180 mesh) abrasives and a 2kg load, showing spalling and deformation of TiC due to abrasion.
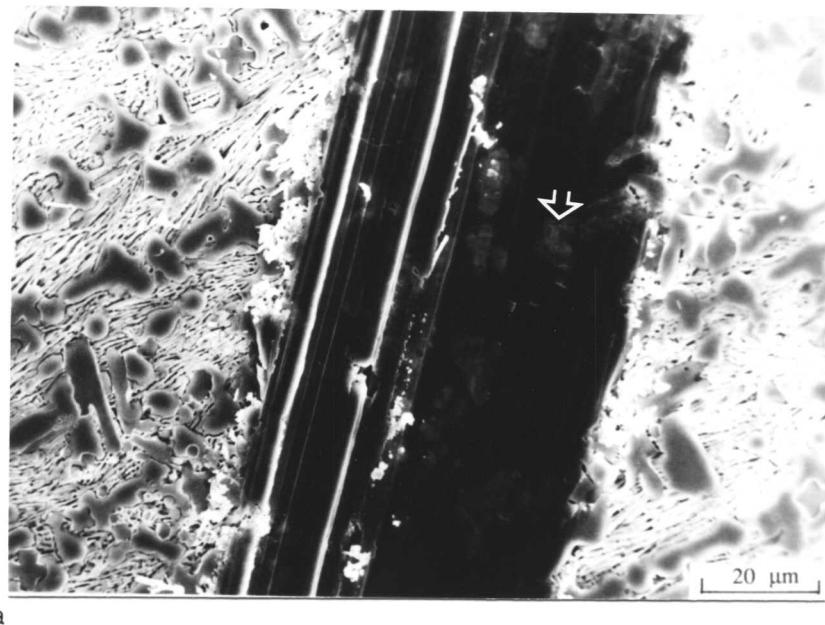
a

b

Fig. 8.6: Scanning electron micrographs after single-pass scratch tests using a Vickers diamond. a) Alloy 79; b) Alloy H3. The eutectic phases are seen to deform plastically and the primary carbides within the scratch groove are cracked (indicated by arrows).

8.1.4 Conclusions

An addition of Ti and Nb to Fe-Cr-C alloys significantly alters the microstructure. The MC type carbides (NbC, TiC) solidify first, followed by the precipitation of austenite dendrites and finally a eutectic decomposition to a mixture of austenite and M_7C_3 carbides. Nb and Ti tie up a large amount of carbon, and decrease the possibility of obtaining a large amount of M_7C_3 carbides. Microanalysis results showed that Nb and Ti are effectively used in the carbide formation with their matrix concentration being very low.

Abrasive wear test experiments using very coarse SiC abrasives (180 mesh) and 2kg load showed that the abrasives are able to deform and cut the carbides. However, scratch groove dimension in the primary carbides was observed to be narrower than the eutectic region due to the high hardness of MC carbides. A great number of work in the literature has shown that these carbides improve abrasive wear resistance of Fe-Cr-C alloy through their high hardness. However, the contribution of MC type carbides to wear resistance must also depend on several other factors such as volume fraction, distribution of carbides, and the strength of the matrix. These factors have not yet been investigated thoroughly.

8.2 Effect of Molybdenum

8.2.1 Introduction

Fe-Cr-C wear resistant alloys have in the past been alloyed with Mo in order to improve abrasion resistance and fracture toughness.[12-15] Although, the wear resistance of such alloys have been studied by several researchers, as discussed in Chapter 6, few have examined the effect of Mo on the microstructure. Even though Mo is a carbide forming element, the presence of molybdenum carbides in high Cr containing iron-based hardfacing alloys is not reported.[12-18] However, Borik and Majetich[9] found very fine Mo_2C carbides, which etched dark in optical specimens of low Mo and high C containing alloys.[1] Energy-dispersive X-ray analysis (EDAX) results from these areas revealed 21.6%Mo and the results were also confirmed using X-ray diffraction. However, the X-ray diffraction results are doubtful since the claimed (10.1) Mo_2C carbide peak is (2.278A) in reality a (44.1) M_7C_3 peak (1.629A).[20] Hence, the only experimental evidence supporting the Mo_2C formation is the EDAX microanalysis results. Similar results have been reported in high Mo and W containing alloys[2] where EDAX microanalysis showed dark etching areas contained 26.7%Mo, and 20.7%W. It was therefore suggested that these regions are $(Mo, W)_2C$ type carbides. Since the probe size is not small enough in scanning electron microscopes to give reliable results from very fine particles, direct evidence of molybdenum carbide formation is not available.

---

[1]

Fe-19.7Cr-5.0C-3.0Mo-0.2Si-0.6Mn
Fe-24.2Cr-4.4C-3.7Mo-1.1Si-0.9Mn (wt%)

[2]

Fe-15.5Cr-4.2C-6.6Mo-3.0W-1.0Si-0.6Mn

Mo partitioning during eutectic growth was studied in high Cr cast irons by Ogi et al.[21] in two alloys containing around 1%Mo.[3] They found that the concentration of Mo in the eutectic M_7C_3 carbides is higher than in the eutectic austenite. They represented the variation of Mo as a function of the ratio of the distance from the centre of the colony to the radius of the eutectic colony. The results showed that the Mo concentration increased gradually from the centre towards the outside and where it reached a maximum value in both the austenite and M_7C_3 carbides. Although they reported that microanalysis experiments in the eutectic austenite and in the carbides were carried out using a finely focussed electron beam there was no information about its actual size.

The most reliable experimental evidence is that of De Mello et al.[19] who studied the solidification sequence of Mo containing white cast irons using Thermal Differential Analysis (DTA). The compositions of the experimental alloys in their work are given in Table 8.3. The microstructure of all the alloys, with the exception of Alloys 5 and 10 revealed primary austenite dendrites and eutectic M_7C_3 carbides. The latter alloys were found to contain primary M_7C_3 carbides and a eutectic mixture of austenite and fine M_7C_3 carbides.

Unidirectional solidification was carried out using Alloys 4 and 7. The only difference between these two alloys is that at the end of recrystallization, different phases, which are located between the secondary arms of the dendrites, are detected. In the alloy 1 (which represents the series I) fine carbides were identified as Mo_2C, and for series II fish-bone-like carbides were identified as M_6C. They reported the presence of strong Mo segregation so that the liquid during dendritic growth is enriched in terms of Mo concentration, promoting the formation of Mo_2C carbides. Note that the experiments were carried out using very slow cooling rates ($\approx 300^{\circ}C/h$) in order to obtain coarse microstructures for easy analysis. Therefore, these results are not comparable with the other experimental works which dealt with relatively high cooling rates.

Generally all the other works in the literature are concerned with the mechanical properties of Mo containing alloys rather than detailed microstructural examinations. For instance, the effect of Mo on hot-hardness was studied by Hagel and Ohriner[18] in Fe-based hardfacing alloys. They compared the hot hardness of Mo and W containing alloys with Co-based alloy which has been extensively used for the hardfacing of poppet-valves. The chemical compositions of the alloys and the hot hardness values as a function of temperature are given in Table 8.4.

3

The compositions of two experimental alloys in the work of Ogi et al.[21]
Fe-14.1Cr-0.83Mo-3.77C
Fe-30.6Cr-0.94Mo-2.89C

Table 8.3: Chemical composition of alloys used in the work of De Mello et al.[19] Alloys 1 to 5 represent series I, and alloys 5 to 10 represent series II.

Alloy	C	Cr	Mo	Mn	Si
1	1.32	6.80	2.38	0.74	0.23
2	1.92	9.65	3.25	1.04	0.45
3	2.74	12.45	3.84	0.92	0.22
4	3.26	16.10	3.14	1.04	0.45
5	3.91	18.75	3.00	1.10	0.61
6	0.92	11.35	2.95	0.74	0.33
7	1.65	16.05	3.20	1.03	0.56
8	2.36	21.40	2.98	1.04	0.54
9	2.74	26.60	2.94	0.98	0.54
10	3.38	32.10	3.01	1.07	0.55

Table 8.4: Chemical compositions of Mo and W containing hardfacing alloys and corresponding hot hardness (HV) values as a function of temperature.[18]

Alloy	C	Mn	Si	Cr	Ni	Mo	W
253	1.90	0.11	0.36	28.0	15.0	5.50	-
4%Mo	1.66	2.75	0.86	29.9	9.70	4.33	-
7%Mo	1.89	0.10	0.10	28.0	13.9	6.85	-
10%W	1.84	0.10	0.15	27.8	15.7	-	9.83
242	1.20	0.50	1.00	30.0	2.25	-	4.50

Temperature, °C

Alloy	20	400	500	550	600	650	700
253	460	368	346	365	310	273	266
4%Mo	428	365	341	325	316	289	277
7%Mo	408	388	371	330	307	270	244
10%W	448	387	375	353	352	337	301
242	440	331	305	306	302	290	239

The hot-hardness of the Mo and W containing alloys was generally found to be higher than that of the Co-based alloy. X-ray diffraction analysis results showed the presence of $M_{23}C_6$ and M_7C_3 carbides in an austenitic matrix. They suggested that this microstructure must provide a greater wear resistance and hot hardness compared to the Co-based alloy. It is interesting to note here that although the Mo content of each iron-based hardfacing alloy is different, there is no systematic variation in hot-hardness values as a function of Mo concentration. Similarly, Charre and De Mello[22] reported that Mo containing carbides (M_6C and M_3C) have a little influence on hardness. On the other hand, it is now appreciated that Mo carbides (e.g. Mo_2C) in steels give rise to a significant increase in hardness.[23] This increase was attributed to the stress field around these precipitates. Such an observation has not been reported in high Cr and high Mo containing irons.

With respect to abrasive wear resistance, De Mello et al.[24] examined variations of the abrasive wear rate as a carbide volume fraction (Fig. 8.7). The abrasive wear rate was found to decrease up to 0.3 carbide volume fraction then to increase. SEM micrographs of the worn surfaces of the Alloys 1, 5, and 9 (Table 8.3) suggested that material removal is mainly a consequence of gross plastic deformation. The results of their wear tests are presented in Fig. 8.7; the minimum in the curve is difficult to understand, but could arise because at high volume fractions the brittleness of the carbides becomes more dominant.
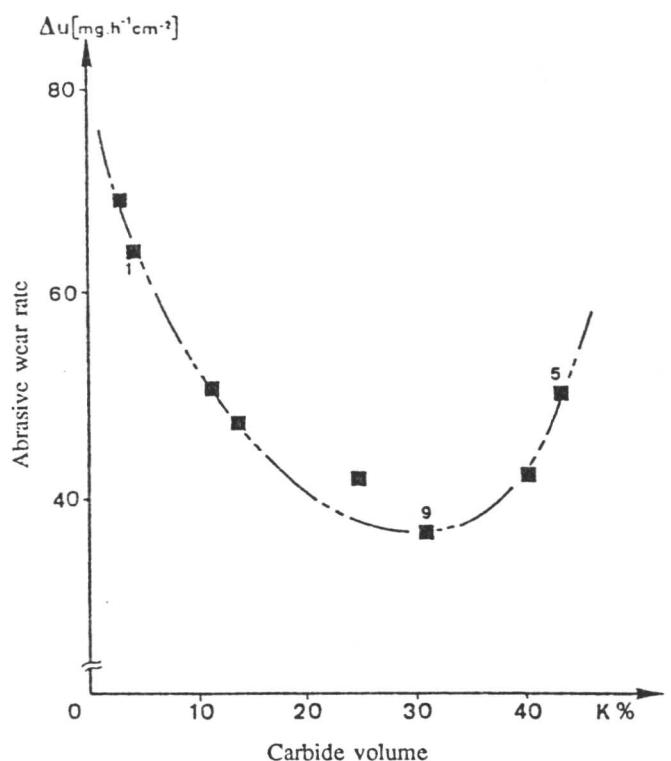

Fig. 8.7: Abrasive wear rate as a function of carbide volume fraction (K) in the work of De Mello et al.[24]

8.2.2 Experimental Results and Discussion

A molybdenum containing Alloy M4 (Fe-31.1Cr-3.61C-8.30Mo-0.32Ni-0.24Si-0.20Mn wt%) was cast by the argon arc melting technique. An optical micrograph of the alloy is shown in Fig. 8.8, which shows a microstructure primary and eutectic M_7C_3 carbides with pro-eutectic austenite dendrites. This micrograph clearly demonstrates the presence of the dark etching regions noted earlier, along the dendrite boundaries.
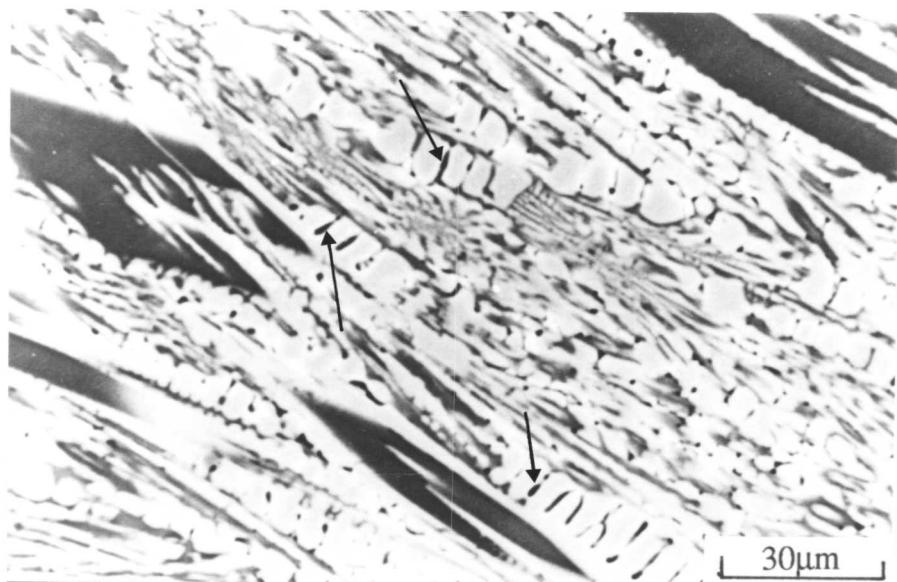
Fig. 8.8: Optical micrograph of alloy M4 (Fe-31.1Cr-3.61C-8.30Mo-0.32Ni-0.24Si-0.20Mn wt%) consisting of primary, and eutectic M_7C_3 carbides with pro-eutectic austenite dendrites. The dark etching regions along the dendrite boundaries are marked by arrows.

Results from X-ray diffractometry are given in Table 8.5. There is no indication of the presence of molybdenum carbides, although they may be present in very small quantity. Thin foils were prepared for transmission electron microscopy and microanalysis experiments. Detailed examination using transmission electron microscopy suggested that the microstructure consists only of M_7C_3 carbides and austenitic matrix (Fig. 8.9). There was again no indication of the presence of molybdenum carbides.

162

Table 8.5: X-ray diffractometry results using CuK_α radiation of the Alloy M4, showing measured 2θ values and corresponding d spacings (Å), and hkl values for the phases identified.

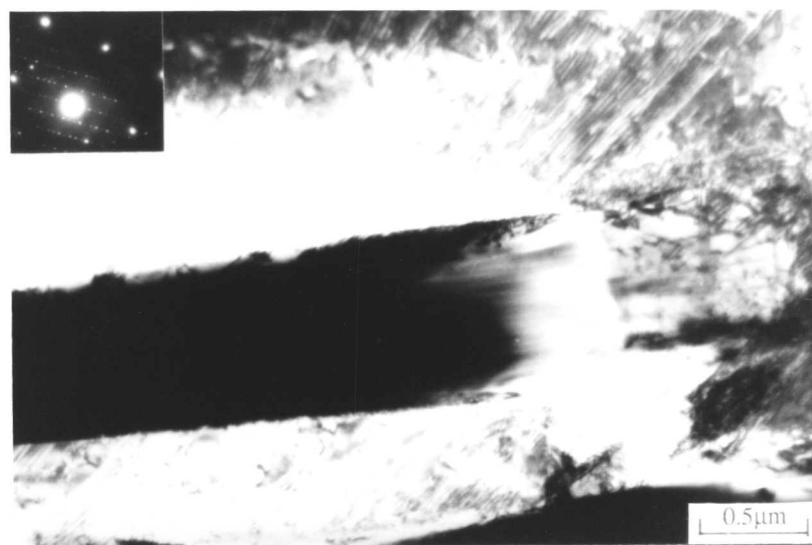| 2θ	d	hkl
39.2	2.298	$24.0_{M_7C_3}$
43.4	2.085	111_γ
44.4	2.03	$24.1_{M_7C_3}$
50.2	1.817	002_γ
52.0	1.754	$44.0_{M_7C_3}$
74.3	1.276	220_γ
82.2	1.172	$01.1_{M_7C_3}$
89.7	1.093	$472_{M_7C_3}$

Fig. 8.9: Transmission electron micrograph of the Alloy M4 showing eutectic M_7C_3 carbide, in an austenitic matrix. The selected area diffraction pattern from the M_7C_3 carbides and austenite is inserted.

Microanalytical experiments were carried out in the eutectic M_7C_3 and austenite using transmission electron microscopy, and in the primary M_7C_3 and around these carbides using scanning electron microscopy and energy dispersive-X-ray analysis. The results (Fig. 8.10, Table 8.6) show that Mo preferentially partitions into the M_7C_3 carbides. Mass-balance equations were used to test the accuracy of the experimental results. It is interesting that the microanalysis results do not satisfy the mass-balance equation for the molybdenum.[4] This suggests the existence of Mo segregation, probably along the austenite boundaries. In fact, microanalysis experiments using scanning electron microscopy showed that the dark etching regions are enriched in Mo, ($\approx$20at%) consistent with the above discussion.

Pin-on-disc abrasion, and single-pass scratch test experiments were carried out. The worn surfaces were found to be similar to that of Alloy 78 which is not an Mo-alloyed deposit. This is not surprising since Mo has no significant influence on the microstructure.

---

[4]

Mass-balance equations for Mo and Cr are written as follows

$$Y_{Mo}^T = Y_{Mo}^\gamma \times V^\gamma + Y_{Mo}^{M_7C_3} \times (1 - V_\gamma) \qquad \dots \dots (1)$$
$$Y_{Cr}^T = Y_{Cr}^\gamma \times V^\gamma + Y_{Cr}^{M_7C_3} \times (1 - V_\gamma) \qquad \dots \dots (2)$$

where Y_{Mo}^T, and Y_{Cr}^T are the average Mo and Cr concentrations (at%) respectively. Y_{Mo}^γ, Y_{Cr}^γ, $Y_{Mo}^{M_7C_3}$, and $Y_{Cr}^{M_7C_3}$ are the mole fractions of Mo and Cr in both phases, and V_γ is the volume fraction of austenite. When the values of $Y_{Cr}^T = 0.29$, $Y_{Mo}^T = 0.043$, $Y_{Cr}^\gamma = 0.22$, $Y_{Mo}^\gamma = 0.024$, $Y_{Cr}^{M_7C_3} = 0.70$, and $Y_{Mo}^{M_7C_3} = 0.039$ are inserted from Table 8.6 in equations 1 and 2. It is clear that mass-balance equation for Mo is not satisfied.
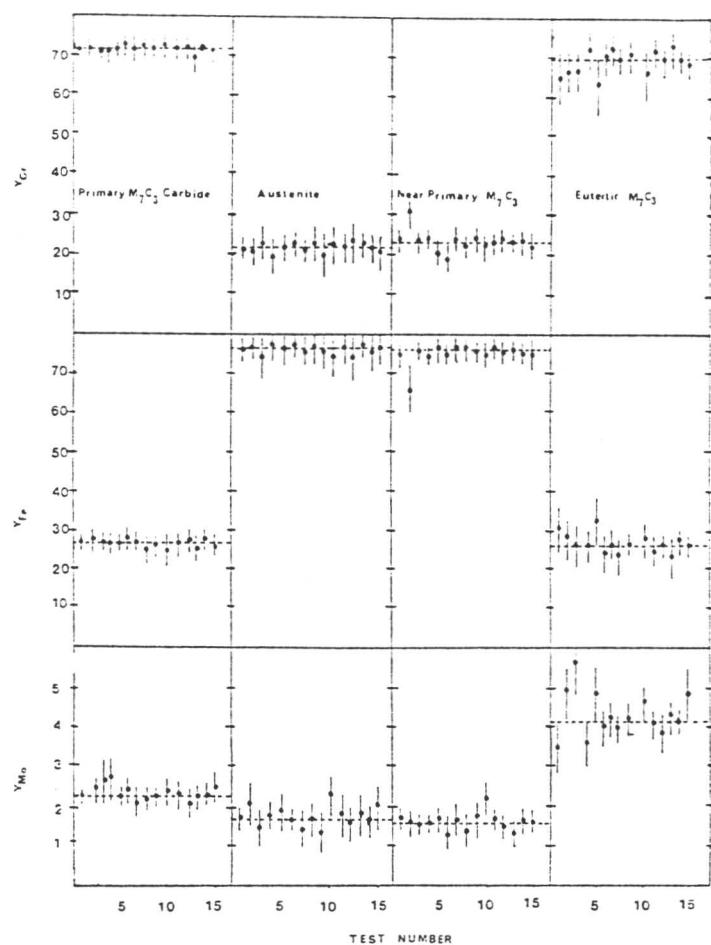
Fig. 8.10: Microanalytical data from Alloy M4 on primary M_7C_3, near primary M_7C_3, austenitic matrix, and eutectic M_7C_3 (at%) when the C is not included (continuous lines show the average values in each phase). The experiments were carried out using transmission electron microscopy, and energy-dispersive X-ray analysis. The experiments near the primary carbides (Near P. Carbide) were carried out using scanning electron microscopy.

Table 8.6: Mean compositions of phases of alloy M4. The results are quoted to three decimal places for internal consistency.

	Primary Carbide		Near P. Carbide		Austenite		Eutectic Carbide	
	Y_i	V_i	Y_i	V_i	Y_i	V_i	Y_i	V_i
Fe	26.254	18.385	75.688	74.250	76.428	75.000	25.903	18.130
Cr	71.363	49.974	22.673	22.250	21.827	21.420	69.997	49.010
Mo	2.283	1.598	1.640	1.609	1.745	1.710	4.100	2.871
C		30		1.899		1.899		30

8.2.3 Conclusions

An attempt has been made to understand the effect of the Mo on the microstructure of Fe-Cr-C hardfacing alloys. A survey of the literature revealed that the influence of the Mo on the microstructure is not well established. Although Mo is a very strong carbide forming and a solid solution strengthening alloying element, it does not seem to have a beneficial effect on Fe-based hardfacing alloys.

Optical microscopy revealed that the microstructure of a cast Fe-31.1Cr-3.61C-8.30Mo-0.32Ni-0.24Si-0.20Mn (wt%) alloy consists of primary and eutectic M_7C_3 with pro-eutectic austenite dendrites. Dark etching regions along the austenite dendrite boundaries were also observed. X-ray diffractometry results showed that the alloy consists mainly of M_7C_3 carbides and the austenite. Detailed microstructural analysis using transmission electron microscopy confirmed this result. However, on the basis of microanalysis data, mass-balance equations could not be satisfied for Mo, perhaps indicating the existence of the Mo segregation. In fact, line trace analysis showed that the dark etching regions are indeed enriched in Mo. However, more work is needed to prove the absence of small quantities of Mo_2C particles.

Tentative results (worn surface examinations) reveal that Mo is unlikely to influence wear properties, consistent with its minor effect on the microstructure.

8.3 Effect of V and W on the Microstructure and Abrasive Wear Resistance

8.3.1 Introduction

Fe-Cr-C type hardfacing alloys are rarely modified with V and W for reasons of cost. Tungsten is generally added as tungsten carbide (WC) particles to an iron-rich matrix.[25] These composite materials are used under heavy abrasive wear conditions due to the high hardness of WC carbides (2400HV).[10] The addition of V to Fe-Cr-C hardfacing alloys have taken a high interest.[9,22,24,26,27] The high abrasive wear resistance of V containing white cast irons has been attributed to the high hardness of vanadium carbides (2660HV)[10]. Borik and Majetich,[9] studied the microstructure and abrasive wear resistance of Cr-free, V-containing iron-based hardfacing alloys and compared them to those containing a high chromium alloy.[5] The microstructure of the vanadium containing alloy was found to contain primary dendritic V_4C_3 carbides (2800 kp/mm^2) in a matrix of austenite, which probably partially transformed into martensite. Comparision was made with a high Cr containing alloy which had a high volume fraction of M_7C_3 carbides ($\approx$0.5) using the pin-on-disc abrasion test under a load of 6.8kg and using 100μm size garnet abrasive. Vanadium containing hardfacing alloys showed the best abrasion resistance. This was attributed to the high volume fraction of (0.36) hard V_4C_3 carbides.

5

     The composition of the experimental alloy deposited by the shielded metal arc welding technique in the work of Borik and Majetich[9]:
     Fe-4.4C-17.5V-7.6W-1.7Si-0.6Mn-0.7Mo-<0.1Cr

The effect of vanadium on the solidification sequence of high Cr white cast irons (1.6-3.6C, and 3.6-16.5Cr wt%) was investigated by Durand-Charre and De Mello.[22] The sequence was not found to change as the V concentration was increased to 6%. Differential thermal analysis showed that the solidification sequence is as follows;

- austenite
- austenite+V_6C_5
- austenite+M_7C_3 eutectic
- austenite+M_3C eutectic (for low Cr and low C containing alloys).

The abrasive wear resistance of the same alloys has been studied by De Mello et al.[24] The chemical compositions of the alloys used together with the volume fractions of the carbides are given in Table 8.7. The microstructural observations showed that the alloys contain V_6C_5, chromium rich M_7C_3, and for low Cr and low C containing alloys, M_3C carbides. Secondary precipitation of V_6C_6 type carbides resulting from slow cooling rates gave rise to a decomposition of austenitic matrix into pearlite, bainite, and martensite. They represented variations of the abrasive wear rate as a function of volume fraction of V_6C_5, and M_7C_3 carbides (Fig. 8.11). In Figure 8.11 the dotted lines show the projections for 0% M_7C_3, and 0% V_6C_5 in order to emphasize the contribution of each carbide to abrasive wear resistance. They suggested that abrasive wear resistance is improved either with V_6C_5 content, or with the total amount of carbide volume fraction (for a given amount of constant V_6C_5 content). However, the results showed that alloy V_A has the best and V_B has the worst abrasive wear resistance (both alloys have the same volume fraction of V_6C_5 carbides) despite the fact that M_7C_3 content in alloy V_A (6.3%) is considerably lower than that of V_B (10.9%). This result is inconsistent with their conclusion. They suggested that this results from the morphological differences. They reported (without any experimental evidence) that the V_6C_5 type carbides in the alloy V_A are more uniformly distributed and more coarser than that of the alloy V_B leading to a higher degree of wear resistance. However, the reasons for the morphological differences were not discussed. In the similar alloys Durand-Charre and De Mello[22] suggested that the addition of manganese leads to a coarsening of V_6C_5 carbides. This is unlikely to be the reason for the formation of coarser carbides in the alloy V_A since the Mn concentration in that alloy is only slightly higher than that of alloy V_B.

Table 8.7: Chemical compositions and volume fractions of carbides in the V containing alloys in the work of De Mello et al.[24]

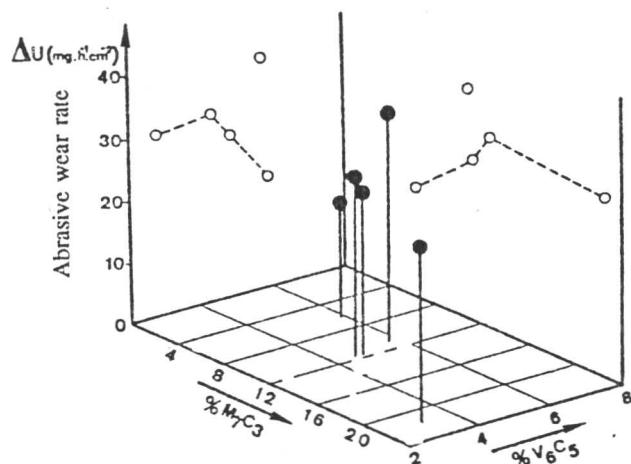| Alloy	C	Mn	Si	Cr	V	%M_7C_3	%MC
V_A	2.21	1.04	0.72	5.99	5.61	6.3	5.8
V_B	2.40	0.92	0.72	8.18	5.91	10.9	5.7
V_C	2.44	0.86	0.66	10.3	6.21	12.1	4.2
V_D	2.66	0.56	0.56	8.18	4.94	11.2	4.7
V_H	3.21	0.59	0.71	8.37	4.89	22.6	2.8

Fig. 8.11: Abrasive wear rate as a function of the M_7C_3 and V_6C_5 carbide surface fraction in the work of De Mello et al..[24] The dotted lines are the projections at 0% of V_6C_5 and M_7C_3 respectively.

168

8.3.2 Results and Discussion

Alloy 37 (Fe-25.77Cr-6.0C-6.31Nb-1.80V-1.50Si-0.80W wt%) was deposited by the manual metal arc welding technique with welding conditions 230A, 23V and with a deposition rate of about 0.004 m/s. The interpass temperature was 500°C. The alloy was deposited in three layers in order to prevent any dilution effect at the top layer. Fig. 8.12a shows the heat-affected-zone (HAZ) and the first layer of the deposit consisting of lenticular martensites along the first layer/base plate boundary and carbon enriched region in the base plate near the deposit. The microstructure of the first layer was found to contain primary austenite dendrites and fine interdendritic M_7C_3 carbides. On the other hand, the second layer has a fine hypoeutectic structure with a large percentage of eutectic matrix (Fig. 8.12b). The top layer micrograph revealed a fairly complex microstructure (Fig. 8.13a). In order to identify the phases present, the backscattered electron imaging technique was applied using scanning electron microscopy on highly polished unetched samples. Fig. 8.13b clearly demonstrates the presence of four different phases in the top layer. The brightest particles are NbC due to the fact that Nb has the second highest backscattered electron coefficient among the alloying elements in the alloy (although W has the highest atomic number, the low W concentration of the alloy ensures that these are not W rich carbides). The grey and dark grey areas probably represent the M_3C and the austenitic matrix respectively. This assumption is consistent with the position of the alloy in the equilibrium isothermal sections of the Fe-Cr-C system (Fig. 7.1). Relatively large black carbides are M_7C_3 type consistent with the microanalysis experiments as will be discussed later.

Microanalysis experiments were carried out using scanning electron microscopy and energy-dispersive-X-ray analysis. The results are presented in Fig. 8.14 and Table 8.8. The large black carbides in the backscattered electron micrograph were found to contain a high amount of Cr ($\approx Y_i = 54$), and Fe ($\approx Y_i = 40$) indicating that these are mainly (Cr, Fe)$_7C_3$ type carbides. Grey areas were found to contain only 10at% Cr and a very high Fe concentration ($\approx$80 at%). This is also consistent with the earlier discussion, suggesting that these are M_3C carbides. It should also be noted that the maximum solubility of Cr in M_3C is 15wt%, supporting the above conclusion. The brightest phases were assumed to be NbC due to atomic contrast and the morphological differences. Microanalysis results show that these particles contain $\approx$60% Nb suggesting that they are indeed NbC. It is surprising that these carbides were found to contain a great amount of Ti ($\approx$21%) even though the Ti was not the alloying element. The Ti distribution was examined by an electron-probe-microanalyser using the X-ray map technique. Fig. 8.15 represents the micrograph and corresponding Nb and Ti X-ray maps. It clearly demonstrates that Ti preferentially partitions into the NbC particles probably due to its MC type carbide forming tendency. Furthermore, it is believed that Ti is dissolved from the coating of electrode during the manual metal arc welding process.[28] Among the alloying elements, V and W were found to partition into the M_7C_3 and NbC. On the other hand, Mo dissolved into the matrix.
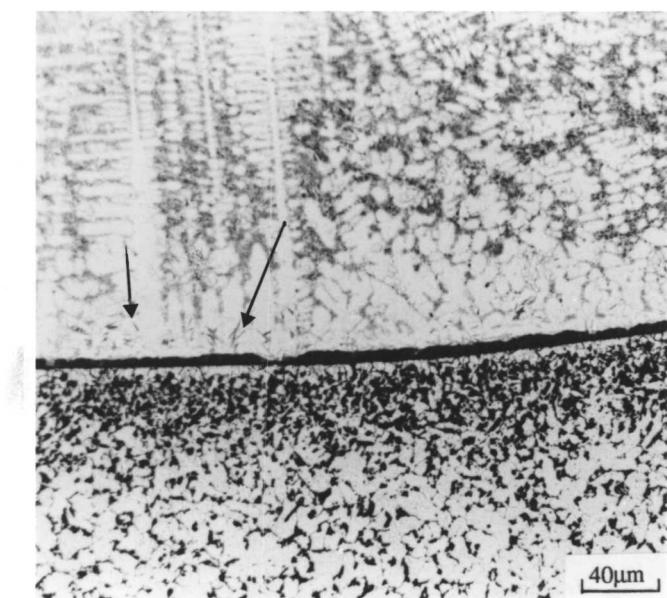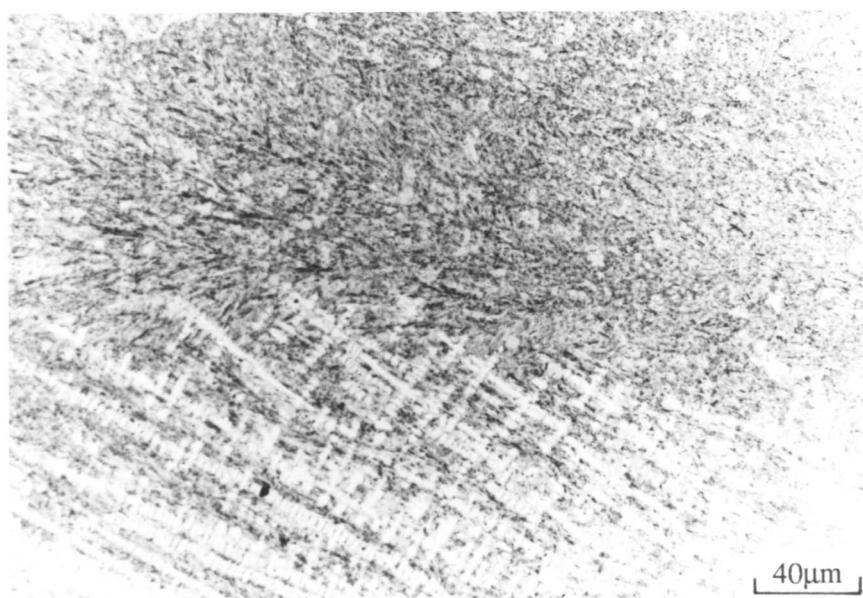
Fig. 8.12: Optical micrographs of the alloy 37, a) Base plate/first layer region consisting of C enriched layer in the substrate along the interface, lenticular martensite in the first layer (indicated by arrows), and growth of austenite dendrites; b) transition region from eutectic first layer to hypo-eutectic second layer.
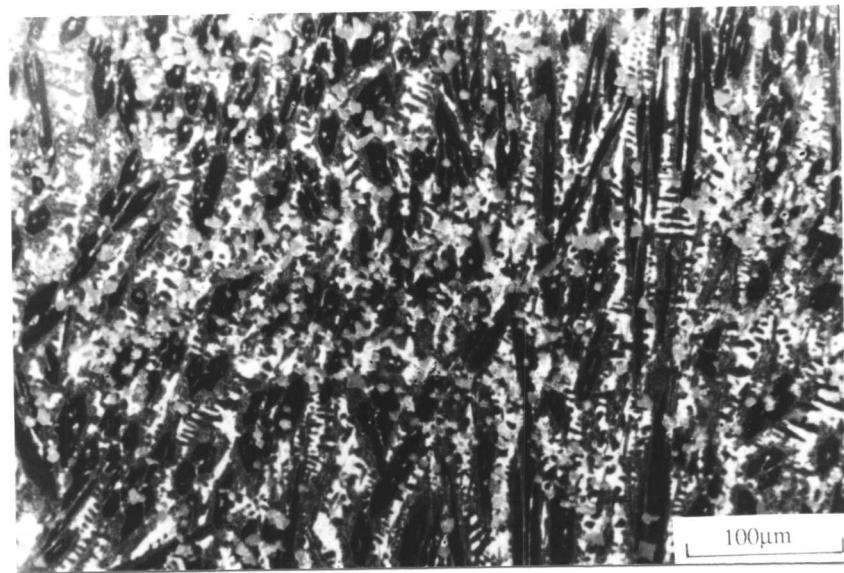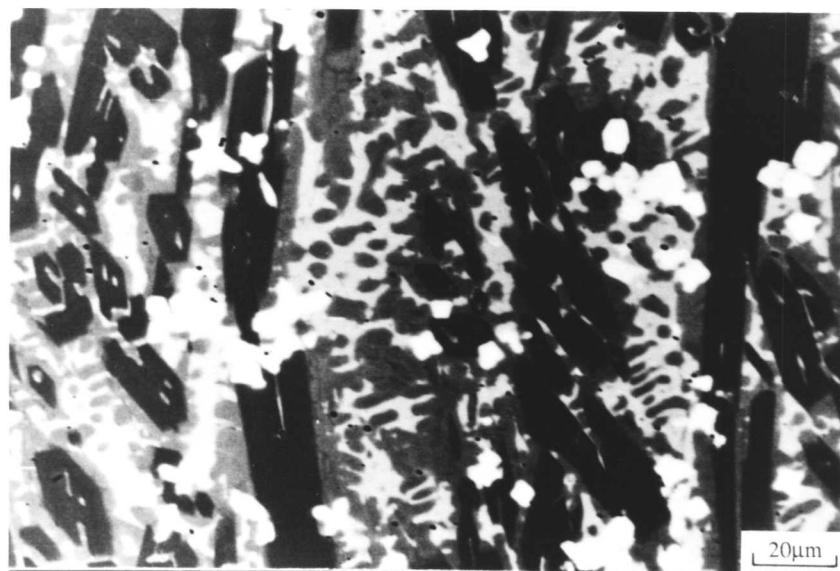
Fig. 8.13: a) Secondary electron image of the top layer of alloy 37 using scanning electron microscopy; b) Backscattered electron image of the top layer of alloy 37 in highly polished without etched specimen showing M_7C_3 (relatively large black particles), M_3C (grey areas), NbC (white particles), and matrix phase (dark grey area).

Pin-on-disc abrasion tests using SiC abrasives (180 mesh) under 2 kg load revealed the presence of continuous grooves and micromachining chips (Fig. 8.16a,b). This indicates that abrasives are able to cut the carbides and plastically deform the structure even though this alloy has a very high volume fraction of carbides.

Single-pass scratch test experiments were also carried out using 500g and 1kg loads. A typical example of the worn surface using a 1kg load is given in Fig. 8.17. Extensive damage within the scratch groove is observed resulting mainly from micromachining processes.

8.3.3 Conclusions

Strong carbide forming elements V and W are rarely added as an alloying element to Fe-Cr-C alloys due to their high cost. These elements form hard primary carbides which in turn improve abrasive wear resistance.

The influence of the V and W on the microstructure and abrasive wear resistance has been studied in Fe-Cr-C-Nb weld deposit containing 1.80V and 0.80W (wt%). The microstructure was found to contain M_7C_3, M_3C, NbC and austenite. Microanalysis experiments showed that V and W preferentially partition into the M_7C_3 and NbC.

High-stress pin-on-disc abrasion and single-pass scratch test results indicated that micromachining deformation process is dominant giving rise to continuous groove formation and carbide cutting.
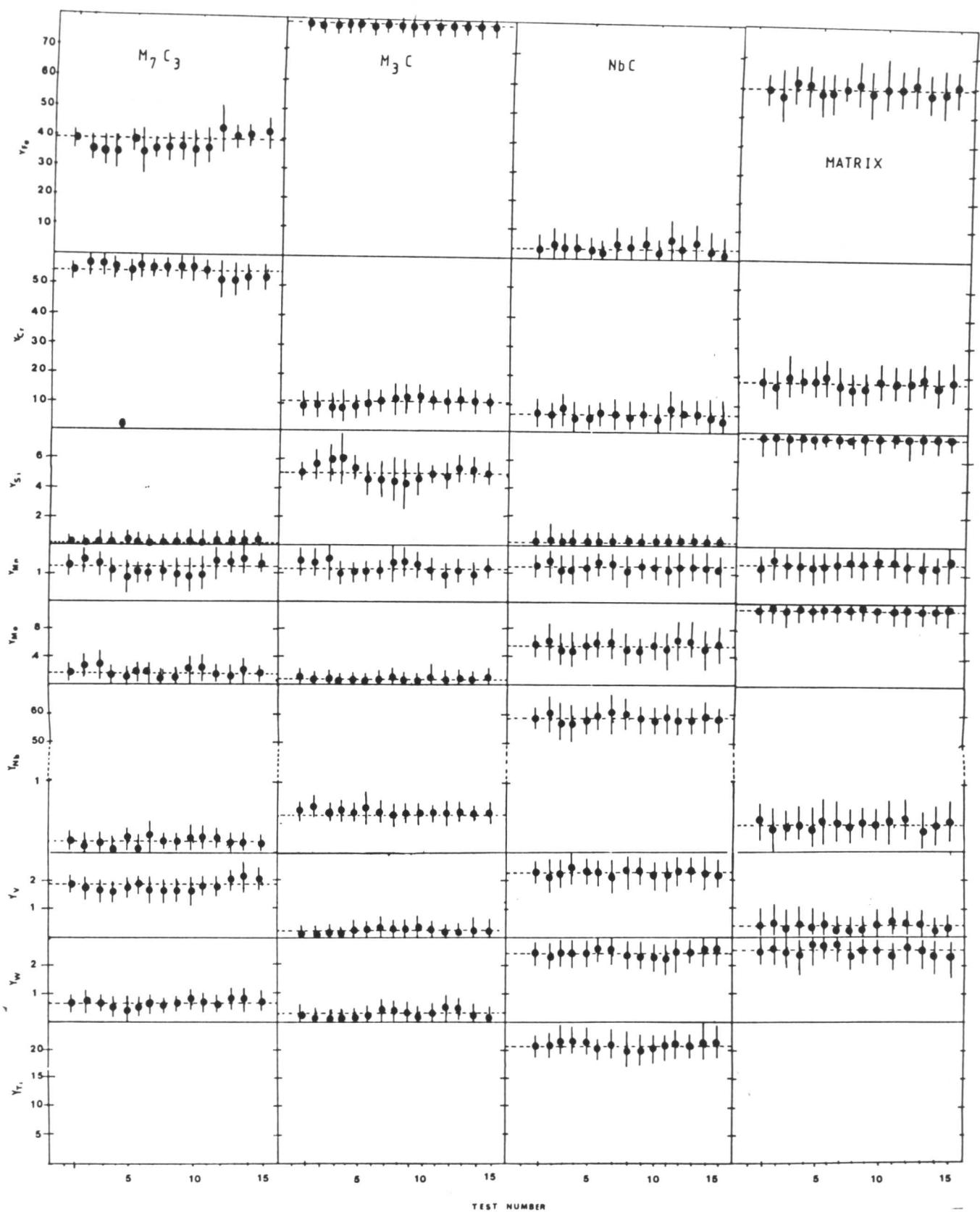
172

Fig. 8.14: Microanalytical data from Alloy 37 on M_7C_3, NbC, M_3C and austenitic matrix (at%) when the C is not included (continuous lines show the average values in each phase). Experiments were carried out using scanning electron microscopy and energy-dispersive X-ray analysis.

Table 8.8: Mean compositions of phases of Alloy 37. The results are quoted to three decimal places for internal consistency.

	M_7C_3		M_3C		NbC		Matrix	
	Y_i	V_i	Y_i	V_i	Y_i	V_i	Y_i	V_i
Fe	39.030	27.330	80.480	60.260	3.185	1.592	59.132	58.067
Cr	54.358	38.060	10.710	8.052	6.117	3.058	17.585	17.274
Si	0.053	0.037	5.688	4.267	0.106	0.053	6.812	6.689
Mn	1.279	0.895	1.173	0.879	0.201	0.100	1.313	1.289
Mo	2.464	1.725	1.801	1.351	5.836	2.918	11.795	11.583
Nb	0.157	0.109	0.540	0.406	58.722	29.361	0.395	0.387
V	1.994	1.396	0.181	0.136	2.328	1.164	0.370	0.363
W	0.666	0.466	0 326	0.244	2.470	1.235	2.574	2.528
Ti					21.483	10.741	0.024	0.023
C		30		25		50		2
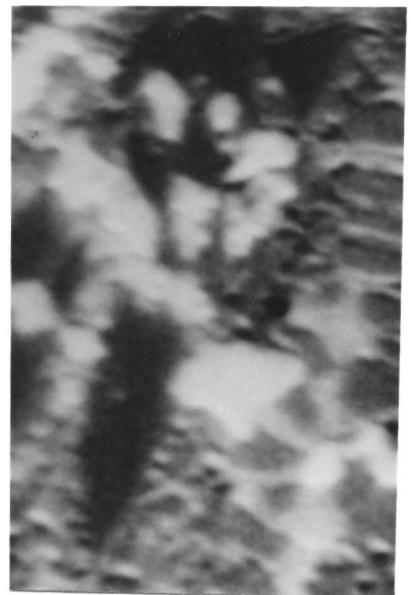
a
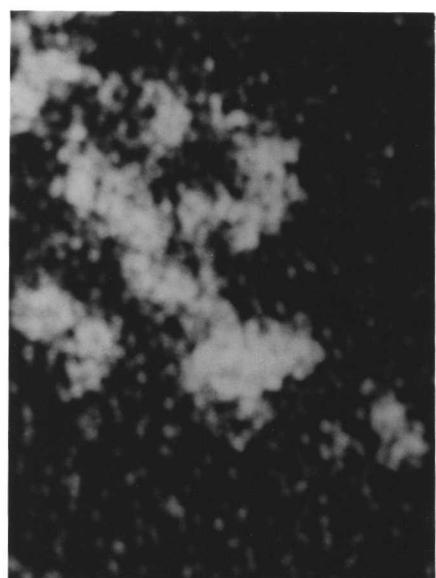
b
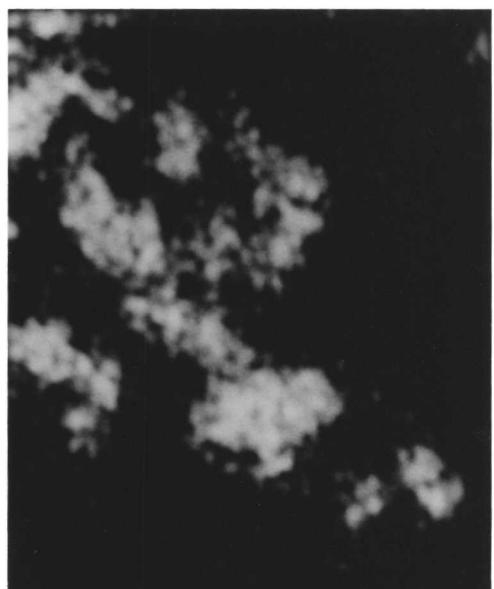
c

Fig. 8.15: a) Electron probe micrograph of the top layer of the Alloy 37; b) corresponding X-ray map of Nb; c) corresponding X-ray map of Ti.

Fig. 8.16: Scanning electron micrograph of the worn surfaces of Alloy 37 after pin-on-disc abrasion test using SiC (180 mesh) abrasives under 2kg load, showing continous grooves and micromachining process.

Fig. 8.17: Scanning electron micrograph of the Alloy 37 after single-pass scratch tests using Vickers diamond showing an extensive damage due to micromachining process.

8.4 References

1) H. BERNS, and A. FISCHER: Harterei-Tech. Mitt., 1982, **37**, 134.
2) N. Sh. SHADROV, L. G. KORSHUNOV, and V. P. CHEREMNYKH: Metalloved. Term. Obrab. Met., 1983, **4**, 33.
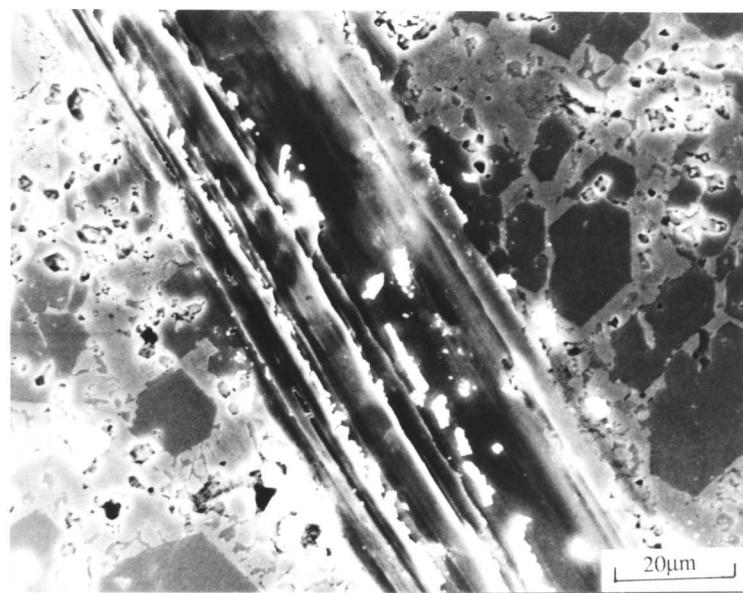3) H. BERNS, and W. TROJAN: Bull. Cercle Etud. Metaux, 1983, **15**, 24-1.
4) W. L. GUESSER: Foundary Manage. Techol., 1985, **113**, 50.
5) N. I. TASHLITSKII, and E. Ya. KOGAN: Vestn. Mashinostr., 1983, **2**, 53.
6) A. SAWAMOTO, K. OGI, and K. MATSUDA: J. Jpn. Inst. Met., 1985, **49**, 475.
7) L. I. AGAPOVA, T. S. VETROVA, and A. A. ZHUKOV: Met. Sci. Heat Treat., 1982, **24**, 364.
8) N. Sh. SHADROV, L. G. KORSHUNOV, and V. P. CHEREMNYKH: Met. Sci. Heat. Treat., 1983, **25**, 284.
9) F. BORIK, and J. C. MAJETICH: in Proc. Conf. 'Wear of Materials 1985', 1985, Am. Soc. Mech. Eng., New York, 595.
10) T. S. EYRE: 'Wear Characteristics of Metals', Source Book on Wear Control Technology, ASM, 1978, pp.1-10.
11) H. BERNS, and A. FISCHER: in Proc. Conf. 'Wear of Materials 1983', 1983, Am. Soc. Mech. Eng., New York, 298.
12) K. H. ZUM GAHR: Z. Metalkde., 1980, **71**, 103.
13) J. K. FULCHER, T. H. KOSEL, and N. F. FIORE: Wear, 1983, **84**, 313.
14) J. D. B. De MELLO, M. DURAND-CHARRE, and T. MATHIA: Wear, 1986, **111**, 203.
15) K. H. ZUM GAHR, and D. V. DOANE: Metall. Trans. A, 1980, **11A**, 613.
16) K. H. ZUM GAHR, and G. T. ELDIS: Wear, 1980, **64**, 175.
17) W. L. SILENCE: in Proc. Conf. 'Wear of Materials 1977', 1977, Am. Soc. Mech. Eng., New York, 77.
18) W. C. HAGEL, and E. K. OHRINER: Moybdenum Mosaic, **6**, 13.
19) J. D. B. De MELLO, M. DURAND-CHARRE, and S. HAMAR-THIBAULT: Metall. Trans., 1983, **14A**, 1793.
20) K. C. THOMPSON, and J. W. EDINGTON: "Practical Electron Microscopy in Materials Science", Monograph 1, 1977.
21) K. OGI, K. NAGASAWA, Y. MATSUBARA, and K. MATSUDA: Bull. Cercle Etud. Metaux, 1983, **15**, 18-1.
22) M. DURAND-CHARRE, and J. D. B. De MELLO: Bull. Cercle Etud. Metaux, 1983, **15**, 19-1.
23) R. W. K. HONEYCOMBE: "Structure and Strength of Alloy Steels", Climax Molybdenum Co. Ltd., 1986.
24) J. D. B. De MELLO, M. DURAND-CHARRE, and T. MATHIA: Bull. Cercle Etud. Metaux, 1983, **15**, 21-1.
25) L. H. PRICE: Metall Process, 1983, 21.
26) G. TUMULKA, and J. SUCHY: in Proc. Conf. '1st International Congress on Heat Treatment of Materials', 1981, Warsaw, Poland.
27) J. DOOD, R. B. GUNDLACH, and P. A. MORTON: in Proc. Conf. 'Mechanical Working and Steel Processing XIX', 1981, Pittsburgh, The Iron and Steel Society of AIME, 475.
28) Private Communication with E-L. SVENSSON.

9. MICROSTRUCTURE, ABRASIVE WEAR RESISTANCE AND STABILITY OF COBALT-BASED ALLOYS

9.1 Introduction

Cobalt-based hardfacing alloys have been used extensively for high temperature applications involving metal-to-metal wear, abrasive wear, impact wear, and for erosion and corrosion resistance. The alloys are generally of the "Stellite" variety, containing large additions of chromium and other alloying elements. The first Stellite alloy was developed in 1900 by Elwood Haynes, with the nominal composition Co-28Cr-4W-1.1C (wt%), now referred to as Stellite 6.[1] Since then, new alloys have been developed, and there are at least 20 Stellite alloys in common use. The alloys can be classified into two main groups;

i) the original Co-Cr-C-W alloys, which are used extensively for elevated-temperature wear applications;

ii) alloys in which the Co, Cr, and W rich matrix has been modified either by the addition of Mo, and Ni or Fe, C, Si and B for high temperature applications involving heavy impact wear conditions.[2]

The microstructures of Stellite alloys vary considerably with composition. They may either be in the form of a hypoeutectic structure consisting of primary dendrites of a Co-rich solid solution surrounded by eutectic carbides, or of the hypereutectic type containing large idiomorphic primary chromium-rich carbides and a eutectic. Among the alloying elements, carbon is found to have a large influence on the microstructure, causing a change from hypoeutectic to a hypereutectic alloy.[3] Carbide forming elements such as tungsten (which forms W_6C type carbides) may reduce the amount of carbon required to reach the eutectic composition. Cr, Mo, and W are found to partition into both the carbide and matrix phases. Solid solution strengthening is also improved significantly by the addition of these alloying elements, and this in turn increases the abrasive wear resistance. The influence of the other alloying elements such as iron and nickel is explained through their effect on the stacking fault energy (SFE).[4][5] The matrix in Co-based alloys can be either in the face centred cubic (fcc), or hexagonal close packed (hcp) form depending upon the chemical composition, temperature and applied stress. It has been reported that the wear characteristics of the fcc and hcp phases are significantly different[6] so that any alloying element which stabilises a particular phase influences the wear resistance. This matter will be discussed in detail later on in the text.

Cobalt-based hardfacing alloys can be deposited by a variety of welding techniques such as manual metal arc (MMA) welding, tungsten inert gas (TIG), and oxyacetylene processes. However, in recent years the use of laser cladding has found many applications in different areas.[7] In this chapter we review the literature concerning the effect of the microstructure on the abrasive wear resistance by considering the effect of deposition techniques. Secondly, the

microstructural characteristics of Stellite 6 alloys deposited by MMA welding, TIG, and laser cladding processes will be examined. Wear test and scratch test results will also be discussed, and the relationship between microstructure and abrasive wear resistance will be considered. Finally, the high temperature stability of the alloys deposited by different processes will be discussed.

9.2 Effect of Carbides on Abrasive Wear Resistance

As discussed in the chapter on iron-based hardfacing alloys, there is no simple proportionality between the abrasive wear resistance and hardness in multiphase alloys. The relationship must partly depend on the behaviour of individual phases. Although the carbides in cobalt-based hardfacing alloys contribute to wear resistance primarily through their high hardness, the volume fraction, shape, morphology, and the strength of the carbide/matrix interface have also been found to play a significant role.[8] Abrasive wear resistance is also strongly influenced by the type of abrasive particles.[8]

9.2.1 Effect of Carbide Size

The effect of carbide size on abrasive wear resistance has been studied extensively in two cobalt-based powder metallurgy alloys, Stellite 6 and Stellite 19.[9][10]1 An advantage of the sintering technique is that it is possible to obtain carbides of different sizes simply by changing the sintering temperature. Scratch tests were carried out by Shetty et al.[10] on two alloys prepared by sintering with microstructures containing fine, medium, and coarse chromium rich M_7C_3 carbides in a cobalt-rich fcc matrix. They performed both single-point and multiple-pass scratch tests by using single quartz abrasive particles and regular-shaped diamonds as scratch tools. Single-pass diamond scratch experiments in relatively large carbide containing alloys showed that the scratch width in the M_7C_3 carbides is smaller than that in the matrix due to the high hardness of the carbides ($\approx$ 1500HV). However, ploughing of the matrix phase indicated that a cutting action is not the only mechanism for removing the entire groove volume. Additionally, some carbide ploughing was also observed at the edges of the carbides as a result of gross plastic deformation. In the large M_7C_3 carbides, cracks, which were perpendicular to the scratch groove direction were observed, and the separation of the carbide matrix interface was seen especially in heavily cracked carbides. On the other hand, in the fine carbide containing alloys the passage of cracks containing several small carbides was observed for both diamond and quartz scratch tools. In both cases, large pits and cracks between adjacent carbides were observed. They suggested that pit formation probably occurs at the places where the average intercarbide distance is smallest, and where a local stress field favours cracking along the carbide-matrix interface. Therefore, the strength of the interface was emphasised as an important parameter influencing the material removal mechanism, especially for the fine carbide containing alloys.

---

1   Stellite 6: Co-28.4Cr-1.35C-4.42W-1.73Fe-1.16Ni-0.98Si-0.04Mn-0.13Mo-0.57B
     Stellite 19: Co-31.42Cr-2.36C-10.08W-1.82Fe-2.0Ni-0.4Si-0.11Mn-6.97Mo-0.19B(wt%).

However, it should be borne in mind that closely-spaced carbides were reported to have a beneficial effect on the abrasive wear resistance by supporting the matrix, and reducing the ability of the matrix to undergo plastic flow.[11] Therefore, the optimum conditions should be examined whilst considering the other factors, such as applied stress, abrasive size, abrasive shape, and matrix phase and carbide/matrix interface strength. For example, if we assume that the carbides are strong enough to resist abrasives, and if abrasives are small, hard and sharp enough to penetrate the matrix phase between two adjacent fine carbides, the material removal mechanism will be controlled mainly by the matrix phase. If the matrix phase is easily abraded, support to the carbides will decrease resulting in a carbide/matrix interface more vulnerable to cracking. Also, if there is poor carbide/matrix bonding, and if local stresses favour initiation of a crack at the interface, then particle decohesion is almost inevitable. On the other hand, if the abrasive particles are not small enough to penetrate a matrix phase between two adjacent carbides, the wear rate will depend on the rate of removal of the carbides. The hardness of the carbide and abrasive, carbide size, carbide volume fraction, abrasive type, abrasive angularity and other parameters then have to be considered in detail. In the work of Shetty et al.,[10] although carbide cracking was observed with both diamond and quartz tools, cracking was much more dominant with the diamond tool. Also, there was no evidence of carbide ploughing and deep cutting of the carbides with the quartz abrasive. This result indicated that if abrasives are harder than carbides, a greater amount of damage would be expected compared with the case of softer abrasives. The abrasive shape also plays an important role. If abrasive particles have a greater angularity, they may cause deep cutting of carbides, which could be spalled off, resulting in a poor abrasive wear resistance.[8]

Shetty et al.[12] have also examined the effect of carbide size on abrasive wear resistance using a scratch test with Al_2O_3 abrasive particles, and a Vickers diamond pyramid.[10] For a structure containing fine carbides, they observed the complete removal of small carbides within chips of debris. For microstructures with coarse carbides, the abrasive particles must cut the carbide phase to remove them since the scratch groove dimensions are smaller than the carbides. In the latter form, wear resistance was found to be greater, although some direct carbide cracking was observed. In the case of coarse carbide containing alloys, micromachining chips were found to be shorter and narrower than that of fine carbide containing alloys. This is experimental evidence for the fact that chip formation is much easier in relatively fine carbide containing materials. Similar results were reported by Desai et al.[9] using low-stress abrasion tests with Al_2O_3 abrasive, and by Kosel et al.[8][13] in the rubber wheel abrasion test (RWAT) by using both Al_2O_3 and SiO_2 abrasives. They showed that in the fine carbide-containing alloys, small carbides are subjected to direct carbide removal resulting in large pit formation and poor wear resistance. Kosel et al.[13] examined the abrasive wear resistance of Co-based alloys that consisted of M_7C_3 and M_6C carbides in the fcc matrix. Using the RWAT with SiO_2, the alloy 98M2 (Co-30.57Cr-2.12C-17.15W-4.04Ni-3.09Fe-3.82V-0.51Si- 0.23Mn-0.24Mo-0.66B wt%), which has both the highest

180

volume fraction of carbides and highest macrohardness, showed relatively poor abrasion resistance compared with the other alloys. Examination of the worn surface suggested that very small M_6C carbides had pulled out, and this probably increased wear rate by contributing additional abrasive particles.

Abrasive wear resistance of cobalt-based alloys has also been investigated when the alloys have been deposited by welding.[14] Among the welding techniques, alloys deposited by oxyacetylene welding were found empirically to be more abrasive wear resistant than those deposited by other techniques.[1][15] For instance, the abrasive wear volume loss of oxyacetylene weld deposits was reported several times lower than that for TIG. This was attributed to the presence of larger carbides, induced by some pick-up of carbon from the oxyacetylene flame. The effect of the carbide size was much more apparent in the work of Antony,[1] who performed the dry sand RWAT in a wrought Haynes alloy 6B, and in a compositionally equivalent Stellite alloy 6 deposited by the gas tungsten arc welding (GTAW) technique. For the wrought alloy, the abrasive wear volume loss was found to be 5-10 times lower than that of the GTAW deposit. He suggested that carbides coalesce, and grow during the hot-working process, leading to higher wear resistance. Similar results were found by Silence,[15] who compared the abrasive wear resistance of Stellite 6 deposited by oxyacetylene and TIG techniques. The abrasive wear volume loss in the oxyacetylene deposit was found to be more than two times lower than that of TIG deposit. Furthermore, when a Haynes Stellite alloy No. 6K (Co-30.12Cr-1.62C-2.09Fe-1.28Mn-0.8Mo-2.37Ni-4.29W) was subjected to different heat treatments in order to compare the effect of average carbide diameter on the abrasive wear resistance, the abrasive wear volume loss was found to decrease with an increase in mean carbide diameter. He suggested that hardness is not a reliable indication of the abrasive wear resistance due to the roughly inverse proportionality between the hardness and the size of carbides. However, in similar alloys it has been shown that the hardness of the alloys was approximately independent of carbide size for a given carbide volume fraction.[9] The increase in the abrasive wear resistance in the work of Silence is probably associated with the increasing ratio between groove depth and carbide size as carbide size decreases.

9.2.2 Effect of Carbide Volume Fraction

One would expect to get better abrasive wear resistance with a higher volume fraction of hard carbides. However, under circumstances where carbides break, spall, or are pulled out, a decrease in wear resistance can be observed due to a high weight loss. A relevant example can be found from a study of six different Stellite cobalt-based powder metallurgy alloys.[13] The alloys consisted of fcc cobalt rich matrix containing solid solution strengthening elements, and M_7C_3, and M_6C carbides. They performed the RWAT with SiO_2 and Al_2O_3 abrasives, simulating low-stress abrasion, and a gouging abrasive wheel test (GAWT), which simulates gouging abrasion conditions using a bonded Al_2O_3 abrasive wheel. In the SiO_2/RWAT and GAWT tests, a minimum in wear rate occured at around 0.5 carbide volume fraction, whereas for the

Al_2O_3/RWAT the weight loss was found to decrease monotonically with carbide volume fraction. The decrease in the weight loss with SiO_2 abrasive after 0.5 volume fraction of carbides was proposed to be due to the interactions between hardness, and carbide size but the interpretation is difficult because the alloy with the highest carbide volume fraction and highest macrohardness also had the poorest wear resistance. Worn surface analysis suggested that very small M_6C carbides are pulled out of the matrix and this decreased wear resistance by contributing to the abrasive particles. The work of Shetty et al.[12] discussed earlier indicates that pit formation at fine particles may also contribute to enhanced wear.

The decrease in the weight loss with increasing carbide volume fraction for Al_2O_3/RWAT was suggested to be dependent on the angularity of Al_2O_3 particles, matrix strength, and abrasion resistance of the carbides. Kosel et al.[13] claimed that since Al_2O_3 particles have a greater angularity than SiO_2 particles, they would penetrate into the matrix phase more effectively. On the other hand, carbides were effectively cut by the Al_2O_3 particles, giving less protection to the matrix. This also emphasises the importance of the matrix strength. Despite the fact that carbides were cut, an increase in the abrasive wear resistance with carbide volume fraction is expected because of a higher hardness of carbides compared with the matrix.

From these discussions it is most probable that the best abrasion resistance can be achieved by large volume fractions of coarse carbides in a high strength matrix. However, as pointed out in the chapter on iron-based hardfacing alloys, optimum conditions should be examined by taking into account the other factors such as carbide/matrix interface strength, carbide spacing, carbide morphology, anisotropy of the microstructure, and matrix behaviour.

9.3 Effect of Matrix

Since the carbides are discontinuous in the structure, support from the matrix is essential. It has been shown that sufficient support by the matrix can prevent pulling out of carbides during abrasion.[16][17][18] In iron-based hardfacing alloys it is now appreciated that abrasive wear resistance is increased significantly when eutectic or primary carbides are well supported by the matrix to prevent cracking and subsequent material removal. In many cases, especially under heavy abrasion conditions, cracks first initiate at the carbide/matrix interfaces probably due to high stress concentrations in these regions. One would think that better abrasive wear resistance could be achieved with increasing microhardness of the matrix phase. However, although the relationship between the hardness and abrasive wear resistance in pure metals is straightforward, there is no simple proportionality for multicomponent alloys. In abraded surfaces strain hardening is always present even though the degree of work hardening depends upon material characteristics. Apparently, strain hardening will increase the hardness of the abraded surface and wear resistance will be better determined by the hardness of the worn surface. In fact, Richardson[19] has shown that wear resistance correlates much better with the maximum hardness of work-hardened surfaces. A good example was given by Shetty et al.[10] representing the influence of the work hardening on the wear resistance. In cobalt-based alloys low-stress abrasion with Al_2O_3 abrasives

was performed before the diamond scratch test in their work. Results showed that the width of the scratches was reduced by a factor of two, due to the work hardening of the surface during the pre-abrasion test.

The strain hardening degree can be represented by the strain hardening coefficient (n). The flow curve of many metals in the region of uniform plastic deformation can be expressed as follows:

$$\sigma = K\varepsilon^n \qquad \qquad .....(1).$$

where σ is the true stress, ε is the true strain, and K is the strength coefficient.

Larsen-Badse[20] attempted to predict the relationship between abrasion resistance, (R), and the surface hardness (H_s) by using equation 1. His analysis yields the following relationship:

$$R = KH_s\exp(n) \qquad \qquad .....(2)$$

He suggested that the wear resistance will be a direct function of the bulk hardness, if the strain hardening exponent is constant between the strain corresponding to the bulk hardness indentation, and the strain corresponding to chip removal.

Strain hardening occurs as a result of interactions of dislocations with each other, and with barriers, which impede dislocation motion.[21] One of the earliest explanation for the strain hardening is that dislocations pile up on slip planes at barriers[2] in the crystal, and produce a back stress, which opposes the applied stress on the slip plane. Possible dislocation interactions and intersecting the active slip plane were suggested as another dominant mechanism for strain hardening. Mechanical twinning, and the presence of hcp platelets may also contribute to work hardening in cobalt-based alloys.[22][23] Experimental evidence exists showing that in Co-Ni-Cr-Mo alloys an increase in the work hardening rate occurs as a consequence of the mechanical twinning, and the strain induced γ-ε martensitic transformation.[24] The effectiveness of each mechanism in terms of work hardening depends upon the strain increment characteristics of each process. This concept was studied by Roebuck et al.,[23] who found the best strengths and ductilities in extruded Co-W-C alloys with the highest fcc content. They suggested that when the fcc phase is stabilised deformation occurs by twinning or slip rather than by γ-ε martensitic transformation. This change in mechanism was thought to be responsible for the highest strength levels, since fcc twinning is more effective than hcp twinning and γ-ε transformation.[3] However, an increase in the strength of the heat-treated alloys was found to be accompanied by an increase in the hcp content. They suggested that hcp platelets create intergranular planar barriers to slip, and leads to an increase in the strength values. In such cases planar faults were suggested as being as important as the relative proportions of fcc and hcp phases.

---

[2] Such barriers could be microscopic precipitates, and foreign atoms, or sessile dislocations, which do not lie on the shear plane and act as a barrier to dislocation motion.

[3] The lattice strains needed to produce a twin configuration are smaller than the strain-induced γ-ε transformation. Therefore, if the strengths of twin interfaces and phase boundaries are equal, twinning produces a higher work hardening rate. If the strengths of twin interfaces in fcc and hcp cobalt are equal, then fcc twinning produces greater work hardening than hcp twinning does, since the rate of the fcc twinning formation is higher than that of hcp twinning formation.

Deformation mechanisms apparently depend upon the applied stress, temperature and stacking fault energy (SFE). For instance, in Co-Ni-Cr-Mo alloys it was shown that at room temperature the γ-ε transformation is induced by plastic deformation for SFE between 10 and 15mJ/m^2.[24] Beyond 20mJ/m^2 twinning occurs and continues as a deformation mechanism up to SFE $\approx$ 50mJ/m^2. It is apparent that SFE has a significant influence in changing the deformation mode. The excellent erosion resistance of cobalt-based Stellite alloys is generally attributed to the low SFE,[25][26][27] which in turn means higher stacking fault probablity and a greater chance for the formation of ε hcp platelets. The lower the SFE (the greater the width of the stacking fault) the more difficult cross-slip is, and is higher the rate of work hardening and the strain to fracture. Bhansali and Miller[25] examined the role of SFE on the galling and wear behaviour of Stellite 6 modified by the addition of Ni, which in turn increases SFE and stabilises the fcc matrix. Their results showed that materials with low SFE tend to strain harden rapidly, and to show the highest galling resistance. However, abrasion wear resistance, and impact resistance were not found to depend on the SFE, because these depend more on the total carbide content, rather than the matrix composition.

Another possible matrix strengthening mechanism is grain boundary strengthening. Grain boundaries act as barriers to dislocation motion, and therefore increase the yields stress. The famous Hall-Petch equation gives this relationship as:

$$\sigma_0 = \sigma_i + k'D^{-1/2} \qquad\qquad .....(3)$$

where σ_0 is the yield stress, σ_i is the friction stress opposing dislocation motion, k' is the unpinning constant, and D is the grain diameter.

The beneficial effect of reducing the primary dendrite arm spacing on the tensile strength.[28] and impact strength[29] is experimentally established. Grain boundaries impede the propagation of deformation-produced microcracks resulting in a high strength. Abrasive wear resistance is found to be better in the finer dendrite containing alloys.[30] Also, in cobalt-based Stellite alloys with laser fused coating the hardness was found to be higher than that of conventional hardfacing deposits. This is attributed to the fine eutectic carbide microstructure resulting from rapid solidification.[31]

Matrix strength can also be increased by solid solution strengthening. Although various factors contributing to solid solution strengthening have been considered, the Suzuki interaction[4] could be an important factor in such heavily faulted alloys. A good example was given by Kosel and Fiore in cobalt-based powder metallurgy alloys Stellite 6, and Stellite 19. The major difference between the alloys was that alloy 19 had a higher amount of solid solution strengthening elements (W and Mo) giving a greater matrix microhardness. Although alloy 19 had a slightly higher carbide volume fraction, the observed greater wear resistance of the alloy 19 was attributed to the higher solid solution strengthening. They also suggested that a high strength matrix can provide a better support to the carbides, and prevent subsequent pulling out of fine particles.

---

[4]   Suzuki interaction occurs primarily as the interaction between partial dislocations and the solute atoms.

The influence of the matrix strength is greater when more angular abrasives are used. The abrasives with a greater angularity can penetrate into the matrix between carbides more effectively than the rounded particles. This may give rise to a less protected carbide, and a carbide/matrix interface which is more vulnerable to cracking.

9.4 Allotropic Phase Transformation and the Influence of Alloying Elements

Pure cobalt exists in two allotropic modifications; it is face-centred-cubic (γ) at high temperatures and hexagonal closed packed (ε) at low temperatures. This allotropic transformation occurs at $417^{\circ}C$ in pure cobalt and the general characteristics of this transformation are:

    - it is essentially athermal in nature, and occurs by shear,

    -during cooling and reheating the transformation is seen to be reversible, on cooling γ->ε occurs at $390^{\circ}C$ and is referred to as the M_s temperature, reverse reaction ε->γ occurs at $417^{\circ}C$ and is referred to as the A_s temperature,[32]

    - the amount of ε depends on the purity and grain size,

    - in pure cobalt, fine grain size inhibits the γ->ε reaction,

    -during transformation surface tilts and upheavels are observed. The crystallographic relationships between fcc and hcp phases are:

$$\{111\}_\gamma//\{0001\}_\varepsilon$$
$$<112>_\gamma//<10\bar{1}0>_\varepsilon$$

The mechanism of martensitic transformation in pure cobalt and cobalt-based binary has been studied by many investigators.[33-37] There are several models which are proposed in order to explain the actual fcc-hcp phase transformation. Basinski and Christian,[35] proposed a model which suggests that, if a major dislocation emerges from hcp lattice, it may dissociate in the fcc region as follows:

$$c \; [00.1] = a/2 \; [110] + a/2 \; [011] + a/6 \; [1\bar{2}1]$$

The first two dislocations are perfect and they can both glide. The third dislocation is the transformation dislocation which moves in the $(111)_\gamma$ plane. As the transformation dislocation rotates about the node, the hcp region is extended by two atomic planes for each complete revolution. But this theory does not explain how the hcp nuclei form, as the authors emphasised in their original paper. Bollmann[33] suggested a model which was based on the intersection of stacking faults. He proposed that if two stacking faults which are differently oriented join to each other, especially when kinetic energy and stress are available, new stacking faults are created due to the localized stress produced at the intersection. The new stacking fault may intersect with another fault, and thus transformation continues by the formation of new stacking faults. Bollmann[33] explained the multivariant transformation in the same sample with this theory, by

185

showing the high stacking fault density in the hcp regions and low stacking fault density in the untransformed fcc region. Fujita and Ueda[37] studied a 18/8 type stainless steel, and proposed a model in which stair-rod cross-slip plays an important role. In this theory, when slip has occurred on the primary slip plane and glide dislocations are dissociated into Shockley partials, under the influence of high stress on the intersecting slip plane, Shockley partials may dissociate into a stair-rod and a Shockley partial glissile. If this process is repeated on parallel slip planes separated by two layers, an hcp region could form. Mahajan et al.[36] studied Co-6.25 Fe (wt%), and proposed a model for fcc-hcp transformation. They suggested that the dislocation reaction

$$a/2 <1\bar{1}0> + a/2 <10\bar{1}> = 3 \ a/6 <2\bar{1}\bar{1}>$$
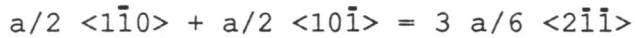
may govern the nucleation of six-layer hcp crystal, and the macroscopic hcp region forms when these nuclei, located at different levels, grow into each other. They explained the coexistence of fcc twins and hcp regions, and orientation dependence of strain-induced hcp martensite with this theory.

Rajan[38] studied phase transformations in a wrought Co-26.7Cr-5.5Mo-0.15C (wt%) alloy. He showed that fcc-hcp transformation occurs in two stages, coincident with a discontinuous precipitation of $M_{23}C_6$ carbides, during isothermal aging treatments at 750°C. He observed a heavily faulted hcp structure, after short time heat treatments, oriented with fcc structure ({0001}hcp // {111}fcc), and after 20 hours another morphology of hcp phase with low fault density appeared. This new form of hcp had no systematic crystallography at its interface with either of the first formed hcp and fcc phases.

The addition of alloying elements alters the thermodynamic stability of the fcc and hcp phases by either enlarging or constricting their fields. These alloying elements will also effect the martensitic transformation by influencing the M_s and A_s temperatures. The effect of alloying additions on the fcc-hcp transformation in cobalt as a function of solubility in fcc cobalt is given in Fig. 9.1.
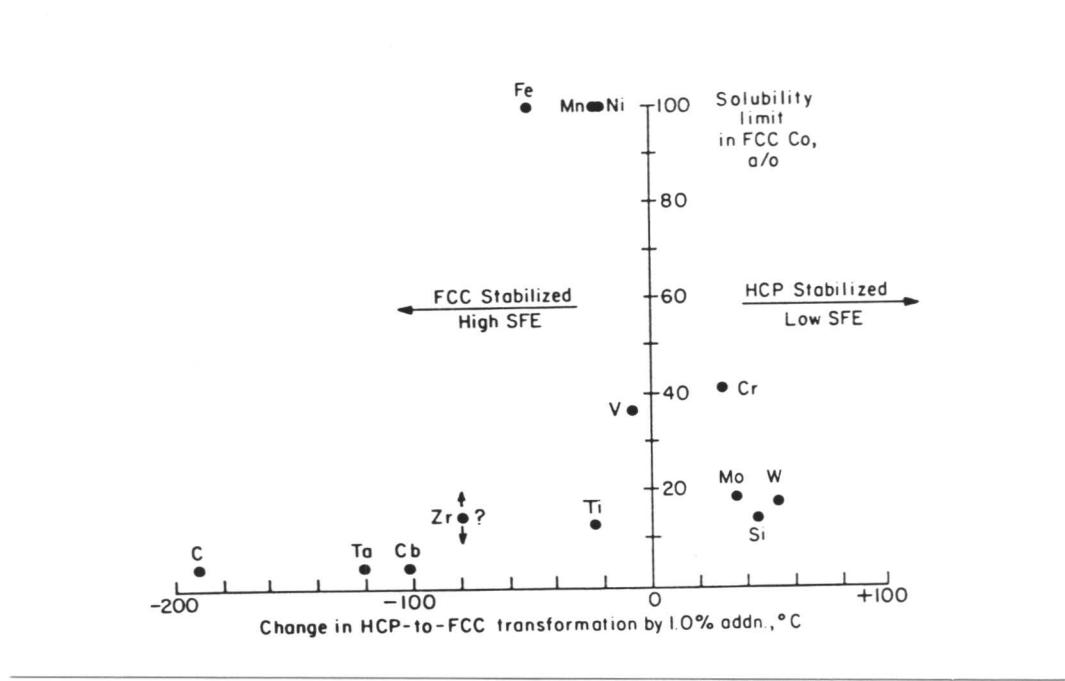
Fig. 9.1 Effect of alloying elements on the fcc-hcp transformation in cobalt as a function of solubility in cobalt.[39]

Ni, Mn, and Fe have a strong effect on the SFE, stabilizing the fcc allotrope, but Mo, W, and Cr tend to stabilize the hcp allotrope and decrease the SFE. Fig. 9.1 has been utilized successfully in the development of cobalt-based superalloys, and it is also a guideline for an alloy selection in hardfacing applications.

9.5 Phase Stability

Cobalt-based hardfacing alloys contain a variety of precipitates such as carbides and intermetallic compounds (e.g. geometrically close-packed (GCP), and topologically close-packed (TCP) type structures). The stability of these phases depends on the bonding mechanism and atomic arrangement. Some cobalt-based hardfacing alloys (e.g. Tribaloy T-800; Co-28Mo-17Cr-3Si wt%) consist of Laves phase which is a type of TCP intermetallic compound. These alloys have been used successfully under heavy metal-to-metal wear conditions. The extent of the stability of the Laves phase and other intermetallic compounds (e.g. sigma, mu, pi) belonging to the TCP structures have been computed by the Phacomp phase computation method.[39] A flow diagram for the Phacomp procedure for superalloys is illustrated in Fig. 9.2. TCP phases are electron compounds in which bonding is promoted by electron vacancies in the 3d subshells of

TCP forming transition metals (e.g. Mo, Cr). Therefore, the procedure is based on the calculation of "average electron vacancy number" as a function of alloy composition and then by establishing a critical number above which TCP phases will be the stable phase. Co-30Cr-4W-1.0C (wt%) alloy was chosen as a reference alloy in this study and the effect of Si, Mn, Mo, Fe and Ni (up to 7wt%) on the probability of TCP phase formation was computed.[5] Electron vacancy numbers of alloying elements are given in Table 9.1. In the reference alloy the microstructure consists of primary γ dendrites and interdendritic M_7C_3 carbides so that electron vacancy concentration of the fcc matrix phase was calculated using the mole fractions given in Table 10.1 for the MMA weld deposit. The results are given in Fig. 9.3. Probability 1 in the figure means that N_v is equal to N_v^{crit} so that any value above that indicates that TCP phase formation is possible. The degree of the stability of the matrix phase is represented by the curve which is below the probabilty of 1; the smaller the probability, the higher the degree of matrix stability. The results are consistent with the observations showing that Si, and Mn are the most effective alloying elements in stabilising the TCP phases among the alloying elements considered.
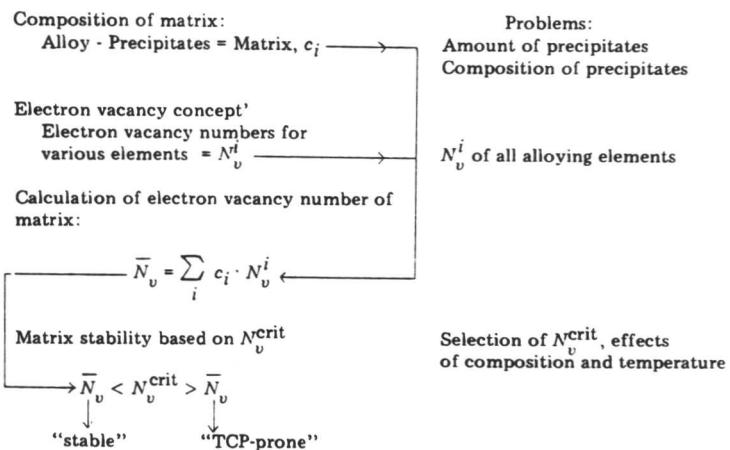
PHASE COMPUTATION METHOD

Composition of matrix:
   Alloy - Precipitates = Matrix, c_i $\longrightarrow$

Problems:
Amount of precipitates
Composition of precipitates

Electron vacancy concept'
   Electron vacancy numbers for
   various elements = N_v^i $\longrightarrow$

N_v^i of all alloying elements

Calculation of electron vacancy number of
matrix:

$$\bar{N}_v = \sum_i c_i \cdot N_v^i \longleftarrow$$

Matrix stability based on N_v^{crit}

Selection of N_v^{crit}, effects
of composition and temperature

$$\bar{N}_v < N_v^{crit} > \bar{N}_v$$

"stable"   "TCP-prone"

Fig. 9.2 Flow diagram for the Phacomp procedure.[39]